

WD-4155 486

ZY IMAGING SYSTEM FOR LAYERED THIN WALL STRUCTURES(U)

AMERICAN SCIENCE AND ENGINEERING INC CAMBRIDGE MA

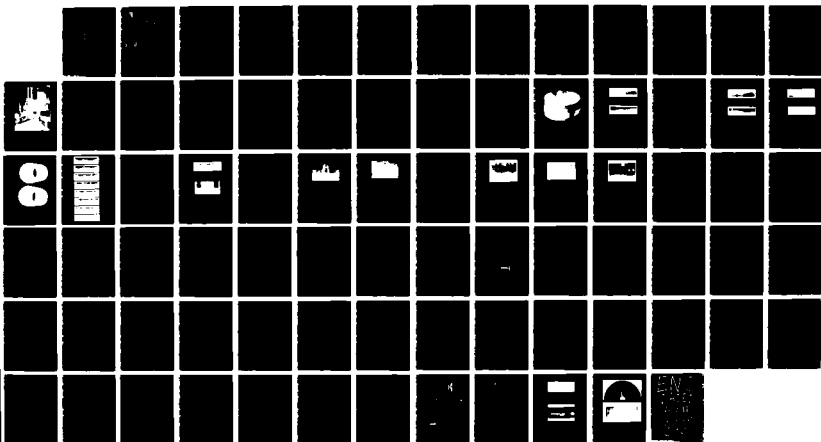
P J BJORKHOLM MAR 88 ASE-5343 AFAL-TR-88-011

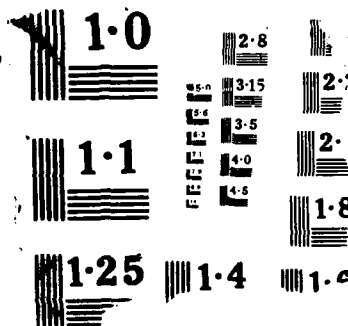
UNCLASSIFIED

F04611-87-C-0049

F/G 14/2

NL





AD-A195 466



AFAL-TR-88-011

AD:

Final Report
for the period
June 1987 to
December 1987

ZT Imaging System for Layered Thin Wall Structures

March 1988

Author:
P. J. Bjorkholm

American Science and Engineering, Inc.
Fort Washington
Cambridge, MA 02139

ASE-5343
F04611-87-C-0049

DTIC
ELECTE
MAY 17 1988
S _{cb} D

Approved for Public Release

Distribution is unlimited. The AFAL Technical Services Office has reviewed this report, and it is releasable to the National Technical Information Service, where it will be available to the general public, including foreign nationals.

Air Force Astronautics Laboratory

Air Force Space Technology Center
Space Division, Air Force Systems Command
Edwards Air Force Base,
California 93523-5000

88 5 16 077

NOTICE


When U.S. Government drawings, specifications, or other data are used for any purpose other than a definitely related Government procurement operation, the fact that the Government may have formulated, furnished, or in any way supplied the said drawings, specifications, or other data, is not to be regarded by implication or otherwise, or in any way licensing the holder or any other person or corporation, or conveying any rights or permission to manufacture, use, or sell any patented invention that may be related thereto.

FOREWORD

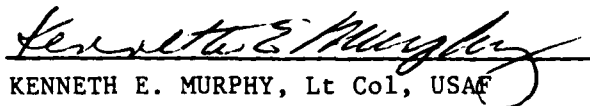
This final report was submitted by American Science and Engineering, Inc., Cambridge, MA on completion of contract F04611-87-C-0049 with the Air Force Astronautics Laboratory (AFAL), Edwards AFB, CA. AFAL Project Manager was Lt Mike Foley.

This report has been reviewed and is approved for release and distribution in accordance with the distribution statement on the cover and on the DD Form 1473.


MICHAEL FOLEY, 1LT, USAF
Project Manager


FRANCISCO Q. ROBERTO
Chief, Propellant Development
Branch

FOR THE COMMANDER


KENNETH E. MURPHY, Lt Col, USAF
Deputy Director
Propulsion Division

REPORT DOCUMENTATION PAGE

Form Approved
OMB No 0704-0188

1a. REPORT SECURITY CLASSIFICATION UNCLASSIFIED			1b. RESTRICTIVE MARKINGS		
2a. SECURITY CLASSIFICATION AUTHORITY			3. DISTRIBUTION/AVAILABILITY OF REPORT Approved for public release; distribution is unlimited.		
2b. DECLASSIFICATION/DOWNGRADING SCHEDULE					
4. PERFORMING ORGANIZATION REPORT NUMBER(S) ASE-5343			5. MONITORING ORGANIZATION REPORT NUMBER(S) AFAL-TR-88-011		
6a. NAME OF PERFORMING ORGANIZATION American Science and Engineering, Inc.		6b. OFFICE SYMBOL (If applicable)	7a. NAME OF MONITORING ORGANIZATION Air Force Astronautics Laboratory		
6c. ADDRESS (City, State, and ZIP Code) Fort Washington Cambridge, MA 02139			7b. ADDRESS (City, State, and ZIP Code) AFAL/MKPB Edwards AFB CA 93523-5000		
8a. NAME OF FUNDING/SPONSORING ORGANIZATION		8b. OFFICE SYMBOL (If applicable)	9. PROCUREMENT INSTRUMENT IDENTIFICATION NUMBER F04611-87-C-0049		
8c. ADDRESS (City, State, and ZIP Code)			10. SOURCE OF FUNDING NUMBERS		
PROGRAM ELEMENT NO. 65502F		PROJECT NO. 3059	TASK NO. 00	WORK UNIT ACCESSION NO. 8K	
11. TITLE (Include Security Classification) ZT Imaging System for Layered Thin Wall Structures (U)					
12. PERSONAL AUTHOR(S) Bjorkholm, Paul J.					
13a. TYPE OF REPORT Final		13b. TIME COVERED FROM 87/6 TO 87/12		14. DATE OF REPORT (Year, Month, Day) 88/3	
15. PAGE COUNT					
16. SUPPLEMENTARY NOTATION					
17. COSATI CODES			18. SUBJECT TERMS (Continue on reverse if necessary and identify by block number)		
FIELD	GROUP	SUB-GROUP			
21	06	2	NDT, NDE, X-Ray, Backscatter, Composite Materials, Delaminations, Tomography.		
14	02				
19. ABSTRACT (Continue on reverse if necessary and identify by block number)					
<p>In Phase I of its SBIR program, "ZT Imaging of Thin Wall Structures" performed for the Air Force Astronautics Laboratory, AS&E demonstrated the feasibility of using a one-sided x-ray backscatter imaging technique called "ZT" to display very small delaminations, cracks, porosity, and chemical species differences in a variety of objects.</p> <p>Using both Air Force supplied carbon composite materials, some with known defects, and AS&E-built custom phantoms, a series of experiments was performed to measure the sensitivity limits of the ZT technique to the various anomalies.</p>					
20. DISTRIBUTION/AVAILABILITY OF ABSTRACT <input checked="" type="checkbox"/> UNCLASSIFIED/UNLIMITED <input type="checkbox"/> SAME AS RPT <input type="checkbox"/> DTIC USERS			21. ABSTRACT SECURITY CLASSIFICATION UNCLASSIFIED		
22a. NAME OF RESPONSIBLE INDIVIDUAL Michael Foley, 1LT, USAF			22b. TELEPHONE (Include Area Code) (205) 275-5183		22c. OFFICE SYMBOL MKPB

The equipment employed for the program consisted of AS&E's laboratory ZT imaging system. During the execution of the program, we modified both the focussing collimator, the detectors and the X-ray beam scanning mechanism to observe the differences in image quality caused by parametric changes in these items. We also examined the objects under inspection using radial, tangential and linear geometries.

The results we obtained confirmed our expectations. Delaminations as small as 127 microns (0.005 in.) deep and 0.05 in. in diameter were imaged with the laboratory system. In the porosity phantom, holes as small as 787 microns in diameter were visualized.

Our density investigations showed the ability to detect density differences as small as 2%. Also uncovered during the density experiments was the sensitivity of ZT to chemical species variations. As a concluding step of the Phase I program, we constructed a mathematical model which accurately predicts total system performance, including the backscatter process and the human detection probability. This model was used to predict the performance of the Phase II system designed as a portion of the Phase I program.

Accession For	
NTIS CRA&I	<input checked="" type="checkbox"/>
DTIC TAB	<input type="checkbox"/>
Unannounced	<input type="checkbox"/>
Justification	
By	
Distribution	
Availability Codes	
Avail	For and/or Special
A-1	



EXECUTIVE SUMMARY

The goals of the Phase I research were to utilize existing AS&E laboratory equipment to determine the limits of sensitivity of ZT imaging to delaminations, porosity, density changes, and chemical changes and to develop a conceptual design for system that would be of significant use to the AFAL in NDE inspection. All of these goals have been met. The Phase II system that is proposed is a dramatic improvement in the sensitivity and utility of this tomographic technique.

Delaminations as small as 127 microns (0.005 inch) deep and 0.5 inch in diameter have been imaged with the laboratory system. This limit may not represent the fundamental limit of the system because of a flaw in the machining of the phantom.

Porosity as such was not easily simulated with a phantom. However to determine sensitivity to small diameter voids, a phantom was constructed with defects of varying depth and diameter. Holes as small as 787 microns in diameter were visualized.

The delamination phantom defined the large area sensitivity of the system and the porosity phantom defined the sensitivity to small diameter voids. In order to use these data to understand the system and to produce a valid scaling law that can be used to predict performance of other designs, we constructed a theoretical model. This simple computer model agrees very well with the observed data and demonstrates that the performance for both phantoms depends simply on two parameters.

We have also completed a conceptual design of a Phase II system that will represent a significant improvement in sensitivity and capability. Its major new features are (1) increased X-ray flux, (2) improved spatial resolution, (3) additional scanning geometries, (4) transmission image capabilities, and (5) a new micro computer based data acquisition and display system.

This Phase II system is predicted to be able to see 25 micron (0.001 inch) delaminations as long as they exceed about 0.5 inch in extent and 1% density variations caused by any form of porosity, chemical species variation or simple mass defects. This system can be completely designed, built, tested and delivered in a 12-month Phase II.

TABLE OF CONTENTS

	<u>Page</u>
EXPERIMENTAL VERIFICATION OF ZT CAPABILITY	1
Introduction	1
Equipment Used	1
Phantom Construction	5
Data Acquisition	7
Phase I Results	8
 THEORETICAL ANALYSIS OF RESULTS	 33
Data Analysis	33
Comparison of Model with Results	36
 CONCEPTUAL PHASE II STUDY	 38
Beam Modulator	38
Phase II System Description	41
Mechanical Hardware	41
Data Acquisition and Display	49
 PROJECTED PERFORMANCE	 53
Projected Performance of the Phase II Conceptual Design	53
X-Ray Flux	53
ZT Collimator Design	54
Pencil Beam Geometry	54
Effect on Detectability	58
 APPENDIX	 59

LIST OF FIGURES

<u>Figure No.</u>	<u>Page</u>
1a. Schematic diagram of the equipment used for Phase I data acquisition.	2
1b. Photograph of the Phase I equipment configured to examine a cylindrical object.	3
2. The ZT scanning geometries used in Phase I:	10
3. AFAL Sample 1.	12
4. Radial geometry scans of AFAL Sample 1, top scan on OD, bottom scan at nominal ID.	13
5. Tangential geometry scans of AFAL Sample 1, top scan focussed on OD, bottom scan at nominal ID.	15
6. Radial geometry scans of AFAL Sample 2	16
7. AFAL Sample 4	17
8. A sequence of 8 tangential geometry scans of AFAL Sample 4.	18
9. A tangential scan of AFAL Sample 4	20
10. The delamination phantom scanned through 0.5 in. of overlying Delrin.	22
11. The porosity phantom scanned behind 1/2 in. of overlying Delrin.	23
12. A scan of the original density phantom with low contrast mixtures of sucrose in each of its six cavities.	25
13. The replacement density phantom	26
14. A scan of the chemistry phantom, slice-centered on the boundary between sample cell and the overlying cover plate.	27
15. Conceptual design for a Phase II system.	39
16. Side view of the proposed Phase II system.	40
17. Phase II System Mechanical Hardware with Cylindrical Test Object.	42
18. Phase II System Mechanical Hardware with Flat Test Object.	43
19. Phase II System Mechanical Hardware Layout.	44
20. ZT "Voxel" Generation	46
21. Inspection Geometries	47
22. Operational Setup for Flat Plate Objects at Various Incidence Beam Angles.	48
23. Systems Data Block Diagram	50

24. Data Acquisition Front End	52
25. This figure shows the X-ray beam profiles at the inspection plane for both the Phase I system (existing) and the proposed Phase II system.	55
26. The Modulation Transfer Function (MTF) for the existign and proposed systems for equally sized beam defining apertures.	56
27. This shows the theoretical output signal from the backscatter detectors as the proposed adn existing beam profiles scan over an edge.	57

LIST OF TABLES

	<u>Page</u>
TABLE 1 SCAN PARAMETERS	30
TABLE 2 AFAL-SUPPLIED SAMPLE	31
TABLE 3 DEFECT THICKNESS	32
TABLE 4 NUMBER OF HOLES VISIBLE IN A ROW	32
TABLE 5 DEFECT THICKNESS	37
TABLE 6 NUMBER OF HOLES VISIBLE IN A ROW	37

EXPERIMENTAL VERIFICATION OF ZT CAPABILITY

Introduction

The technique of backscatter tomographic (ZT) imaging has been discussed in detail in the Phase I proposal and in the literature and will not be repeated here. However, a paper describing the technique is included in Appendix A for review if desired.

The first section of the Phase I work was directed towards verifying the ZT capability for imaging defects in thin walled carbon structures. Three classes of objects were scanned: (1) Two filament wound carbon cylinders with no known defects, (2) one carbon-carbon cylinder with a visible but unquantified defect, and (3) phantoms which simulate delamination, porosity, density variations, and chemical species variations.

Equipment Used

This phase strictly utilized existing equipment in the AS&E imaging laboratory. The equipment was specially configured, however, for this particular problem and is shown in Figure 1.

The source of X-ray for the system is a Dynamax Model 79B Machlett tube with rotating anode. It is sealed in a housing which has a circulating oil heat exchanger for cooling. A heat capacity meter monitors the power dissipation. Power is supplied to the tube by a Deltaray Corporation high voltage power supply. Typically this is run between 90 kV and 100 kV at 10 mA current.

Two collimators were used in this program. The first was an existing collimator in use prior to the start of this program. It had a focal length of 5.625 in. and an efficiency, which when coupled with the first version of the chopper wheel, required 20 minutes to make a scan.

During the conduct of the Phase I experimentation, AS&E built and installed a new collimator with a 2.9 inch focal length and an increased detector effi-

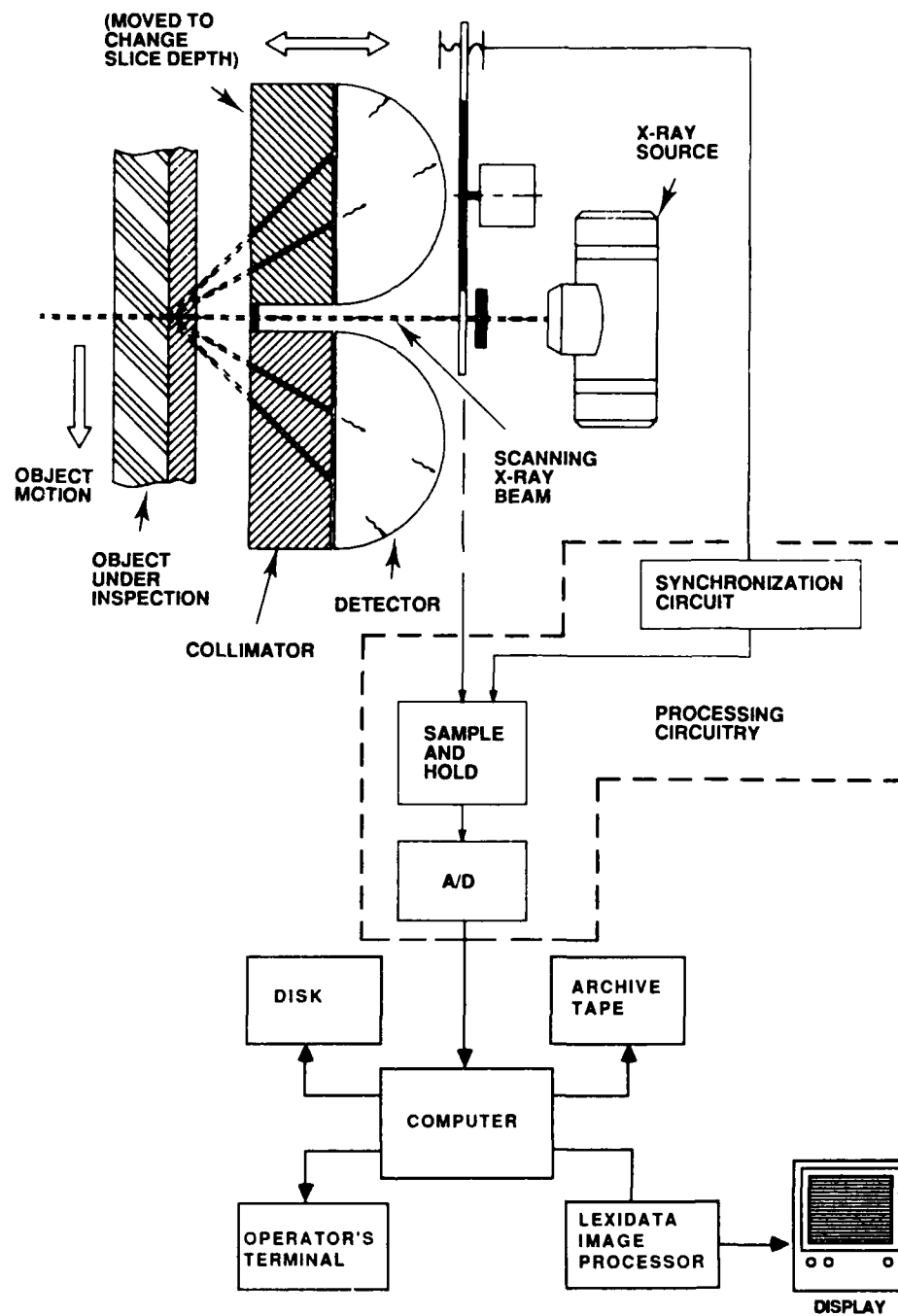


Figure 1a. Schematic diagram of the equipment used for Phase I data acquisition. Only the high voltage power supply which runs the X-ray tube is omitted.

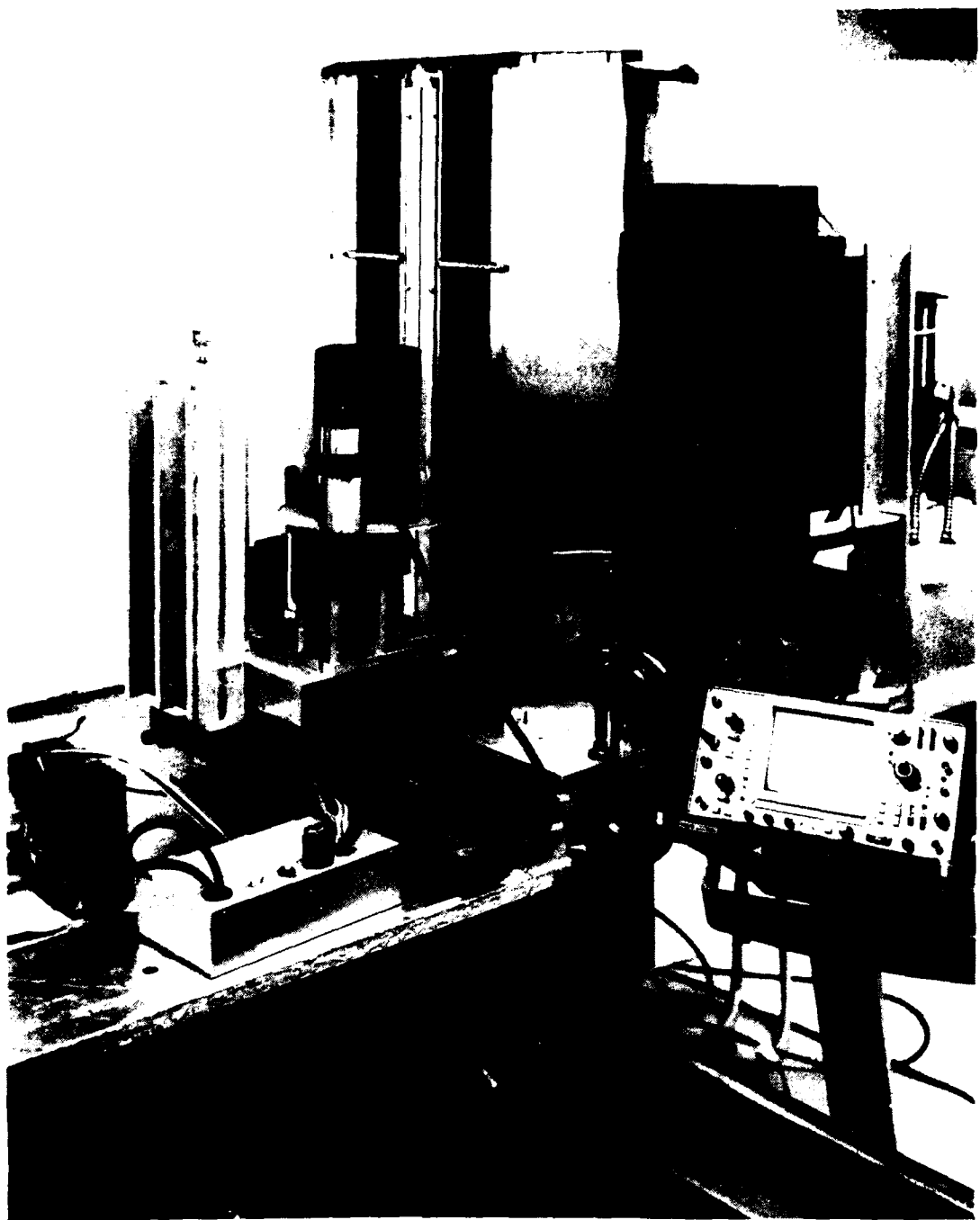


Figure 1b. Phase I equipment configured to examine a cylindrical object. The ZT collimator is the large object nearly in the center of the photograph. The X-ray source housing and the chopper wheel are located behind the collimator and the object to be inspected is located in the front of the collimator.

ciency. Together with the latest version of the chopper wheel, only 16 scan lines were required to be added for good statistics.

The number of lines added during a scan is dependent on the efficiency of the detectors and the collimator. The more efficient the detectors and collimator, the fewer lines have to be added together to get good statistics for imaging.

The data from the A/D were handled by a Data General Nova computer operating under Mapped Eclipse RDOS Rev. 7.20. The computer supports one hard disk drive which holds the OS, utilities and Data Acquisition software and the on-line image files. Also, there is a 1600 bpi tape drive for use in archiving images from the disk to free up space for later scans. The existing software also allows one to retrieve images from tape provided there is an available image slot on the disk.

Data are displayed to the operator by means of a standard terminal. Images are displayed by writing the image file to a Lexidata System 3400 image processor, which displays the image on a high resolution, black and white non-interlaced monitor. The computer can also read the data to perform operations such as area averaging. Software controls which were used in this project were simple contrast enhancements or gray scale stretching. Features not visible on the initial display image could be seen with adjustments of the contrast.

Since ZT imaging requires relative X-ray/object motion, two translation stages were used. The first was a linear translation stage. It was equipped with a variable speed drive, capable of speeds slower than 0.013 in./sec. The table moves in one dimension, that being perpendicular to the incident X-ray beam.

The second was a rotational stage. It was built to allow scans of the cylindrical phantoms to be made. It had 2 micrometer adjustable axes: one along the X-ray beam (Y) and one perpendicular to the beam (X), as well as a coarse Z adjustment to place the sample vertically for a scan.

Phantom Construction

Evaluation of the ZT system for porosities, delaminations, chemical and density variations required the construction of phantoms having known values of these defects. The statement of work called for measurements of these artifacts with the following parameters:

1. Delaminations with thicknesses of 1000, 500, 250 and 125 microns. Four of each thickness are to be placed 0.5, 1.0, 1.5 and 2.0 inches below the surface of the phantom.
2. Density fluctuations in the amounts of 10, 5, 2, 1 and 0.5% to be located at any depth convenient.
3. Porosities of holes with varying mass defects will be included down to and inclusive of 0.5% mass defect.
4. A known chemical species variation phantom.

It was intended that these phantoms be constructed of carbon-carbon composites, but due to the difficulty in obtaining materials required, alternate substances were utilized.

The delamination phantom consisted of 1/2 in. diameter holes milled to depths of 0.080, 0.040, 0.020, 0.010, 0.005 and 0.0025 inches. These were placed along the center line of the block. Note that this included one thicker and one thinner delamination than was originally specified.

The porosity phantom was constructed as a 4 x 9 array of holes. Diameters of the holes in each of four rows were 0.250, 0.171, 0.125, 0.088, 0.062, 0.044, 0.031, 0.022 and 0.018 inches. The depths in the four rows were 0.200, 0.120, 0.040 inches and depth equaled diameter.

The chemical/density phantoms were initially a two-piece design. One piece was a front plate which was to be glued onto the other piece sealing the

assembly. The other piece had six 1/2 in. diameter holes milled to a 1/4 in. depth. Filling holes were drilled into the cells from what was to be the top of the phantom.

This phantom was first made of a readily available material, black delrin. This material has a density, as measured, of 1.47 gm/cm^3 and was chosen to simulate the density of carbon-carbon composite. It is also easily machinable. Phantoms were made in the porosity, delamination, chemical/density configurations (see diagrams). Scans were made of the porosity and delamination phantoms using the 3 in. focal length collimator. Problems arose in the chemistry/density phantoms however. It had proved impossible to dissolve the required amounts of chemical and sucrose to match the density of the delrin.

Two additional phantoms of the chemical/density configurations were then made out of Lexan which has a density of 1.24 gm/cm^3 . The solutions of chemicals, namely sucrose, zinc chloride, potassium iodide, and calcium chloride, were able to be mixed to the required density. Scans were then made of these phantoms using the 3 in. focal length collimator.

A third density phantom was then made from lucite, density of 1.157 gm/cm^3 , such that no gluing would be required. This was also scanned with the 3 in. focal length collimator.

Five of the cells contained measured densities for this set of scans. They were 1.167, 1.159, 1.150, 1.00 and 1.154 gm/cm^3 , respectively, for cells 1, 2, 3, 4 and 5. The densities represent the mass density contained in each cell which is made up in part by a density of sucrose and in part by a density of water. The actual amounts of sucrose dissolved in the water varied as 100%, 95%, 90%, 0% and 92.5% as measured relative to the densest solution.

The first set of scans of the density phantom were taken with densities of 1.167, 1.166, 1.165, 1.163, 1.159, 1.150 and 1.134 gm/cm^3 . These ranged as 100% for the 1.16 gm/cm^3 to 97.14% for the 1.134 gm/cm^3 . The scans showed a difference between the background and each cell. Since the solutions were made by cutting a stock solution of 1.167 gm/cm^3 with water, and could be inconsis-

tent, new solutions of sucrose were made by dissolving well known amounts of sucrose in a specific amount of water, so each cell was filled from a 'stock' solution.

The chemical phantom showed no signs of the dark rings around the cell and so the lexan assembly was used. The samples of chemicals were mixed to the density of the lexan 1.24 gm/cm^3 . Four chemicals were used, those being sucrose, potassium iodide, calcium chloride and zinc chloride. The two remaining cells were left empty.

Data Acquisition

Data were obtained of the planar phantoms (i.e., chemical, porosity, density, and delamination) by use of a translation table which moved perpendicularly to the direction of the beam. The sample was placed at selected positions in front of the collimator so as to allow imaging of different layers into the phantom. For instance, the chemical phantom was scanned at 5 levels relative to the cell containing the samples (center of cell, front/back walls of cell, and in front, behind cell).

The porosity and delamination phantoms were also scanned through varying thickness of material. These would correspond to depths of $1/8$, $1/4$, $1/2$, 1, 1.5 and 2 in. These scans were done to show the sensitivity of the system to these defects.

The large radius carbon-carbon phantom supplied to AS&E by the Air Force at the start of the project was also scanned "linearly" but on two axes parallel to the surface. Scans were performed using the 5.5 in. focal length collimator at a translation speed of approximately 0.04 in./sec.

Each planar phantom was held in place with a clamp and positioned such that the image slice was at a constant depth relative to the surface. This also insured consistency in positioning if work was needed in or around the area.

Data taken on the circular phantoms supplied by the Air Force, i.e., 5 in. AF phantom, 8 in. AF phantom and the government-supplied carbon fiber cylinder with known delaminations, were taken using a rotating stage and two geometries. Data was taken using the 5.5 in. focal length collimator on all three samples.

The samples were set on the stage and aligned with the concentric rings scribed into its table. Two markers, one of solder and one a paper clip, were attached to the cylinder being scanned as reference marks. The 5 in. and 8 in. AF phantoms were scanned using the outer surface of the cylinders as the radial reference R_0 . These were scanned throughout their entire thickness in steps of 0.020 in. for the 8 in. and 0.050 in. on the 5 in.

Rotational speeds were set in accordance with the efficiency of the detector. The 5.5 in. collimator required times of 1200 sec to scan an object. This corresponded to a rotation of 0.3°/sec. The actual linear speeds of the cylinders varied as a function of these radius according to:

$$S = d \theta R$$

which means for a large radius, a longer segment moves through the imaging region in a given time than does for a smaller radius.

Initially scans were made in only one geometry, with the beam coming into the sample radially. Some thought was given as to the possibility of structure or defects hidden under the markers used for orienting the image. Since the solder blocked the X-rays, there were parts not being illuminated due to the shadow. An approach whereby the cylinder is illuminated by the X-ray beam tangentially would allow those areas lying in the radial shadow to be illuminated. As the beam and imaging detectors were both lying along the same axis, both the illumination and imaging can be considered as tangential in this case.

Phase I Results

During the course of Phase I, ZT scans were made of the phantoms described in above and of several composite structures provided by AFAL in accordance

with Modification P00001 of the contract. Table 1 gives the mechanical and operational parameters employed for the scans. Part A of the table applies to all of the scans reported in this document. Part B describes properties of the ZT collimator and sampling as they were configured for early scans during the program, while Part C describes them after improvements were made. In presenting results in this section, the ZT collimator employed will be identified with reference to the table and "Type B" or "Type C."

In general, scans were done using the maximum available X-ray flux, i.e., at the maximum kilovoltage at which the X-ray tube would operate without arcing and at the maximum fluoroscopic (steady state) current usable at that kilovoltage. For the Type B scans, we always acquired data for 844.8 seconds, corresponding to 3.22 millisecon for each of the 512 x 512 pixels. These scans were acquired by adding many (396) rapid sweeps of the pencil beam. For the Type C scans, besides using an improved collimator design, we added a relatively small number (16) of slow sweeps for a total acquisition time of 512 seconds or 1.95 millisecon per pixel. Therefore, we traded off some of the improved collection efficiency of the new ZT collimator for reduced scan time. The image signal-to-noise ratio (S/N) is proportional to the square root of the imaging time, so the net (S/N) was reduced to

$$(512/844.8)^{1/2} = 78\% \text{ of what it would have been for equal scan times}$$

The primary reason for slowing the sweep rate was to reduce vertical streaking related to afterglow in the detector scintillator. Results will be presented that confirm this prediction.

Scans were made in one of three scan geometries as illustrated in Figure 2. Figure 2a illustrates what we have designated a "radial" scan for cylindrical objects. It obtains a "slice" which is really an annular ring from within the wall of the cylinder. Its resolution within the slice is characterized by the dimensions of the scanning beam, about 1 mm by 1 mm, while the slice thickness is determined by the properties of the ZT collimator and is actually spread over somewhat more than 1 mm.

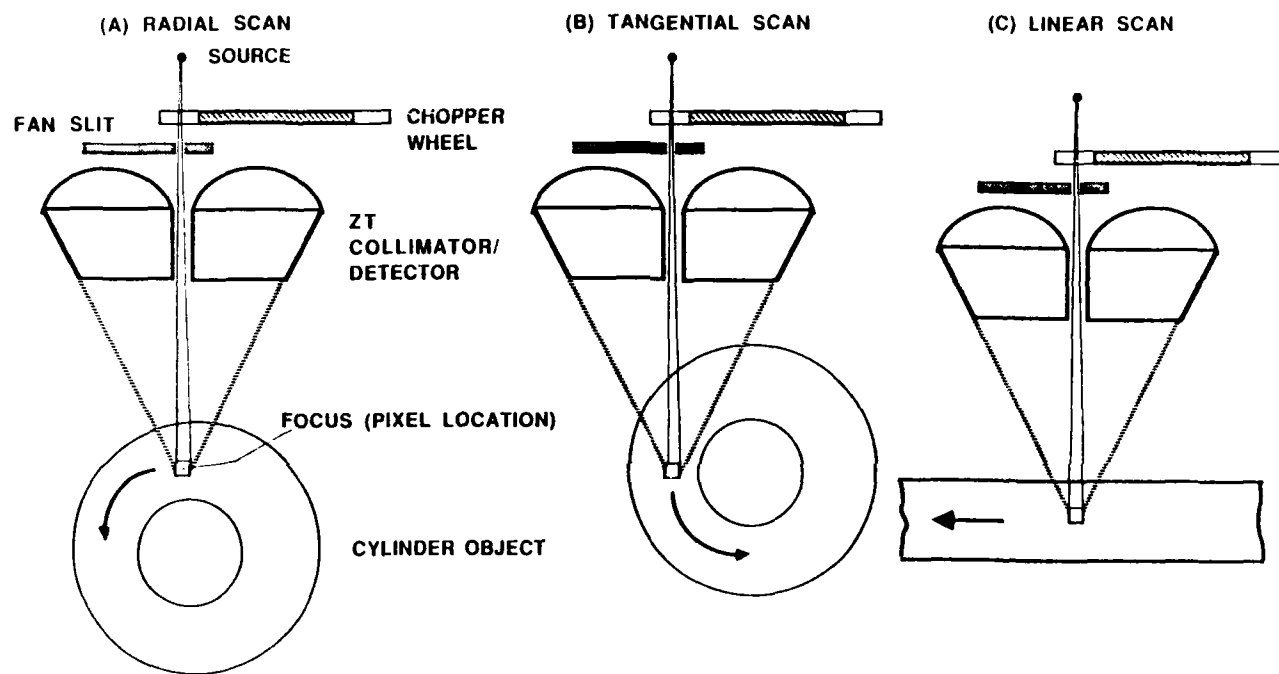


Figure 2. The ZT scanning geometries used in Phase I:

- (a) Radial
- (b) Tangential
- (c) Linear

Figure 2b illustrates a "tangential" scan for cylindrical objects. It also gives an annular slice, but in this case the slice thickness is sharply determined by the fan beam slit, about 1 mm in the scans reported. This geometry has significantly better sensitivity for circumferential cracks or delaminations. Furthermore, the resolution can be sharpened simply by reducing the slit size, a feature which is not possible when the ZT collimator defines the slice thickness.

In both of the cylinder scanning geometries, the slice "plane" (or annulus) is changed by shifting the center of rotation relative to the ZT focus.

Flat objects were scanned using a linear translation stage as shown in Figure 2c. This geometry is analogous to the radial geometry for cylinders and has similar characteristics for slice thickness. Although it was not implemented in Phase I, it is feasible to do scans of flat objects by a method similar to the tangential scan for cylinders, thereby achieving better delamination sensitivity, and this feature is presented in the Phase II plan.

AFAL-Supplied Objects

Four sample composite structures were provided by AFAL and were scanned as part of the Phase I effort. A summary description of the four samples is given in Table 2. Although the scans of these objects are of interest for comparison purposes and because they are real structures instead of phantoms, they contain no defined or "calibrated" defects. For that reason, the results can only be interpreted qualitatively.

AFAL Sample 1. A photograph of this object is shown in Figure 3. It was scanned using the Type B collimator of Table 2. Seven (7) radial geometry scans were done, at 0.05 in. (1.25 mm) radial increments and six (6) tangential geometry scans were done at the same increments.

Figure 4 is a hard copy of two of the radial scans (a) being near the outer radius and (b) near the inner radius. R_0 refers to the cylinder outside radius. The images show about 80% of the annular slice circumference, pre-

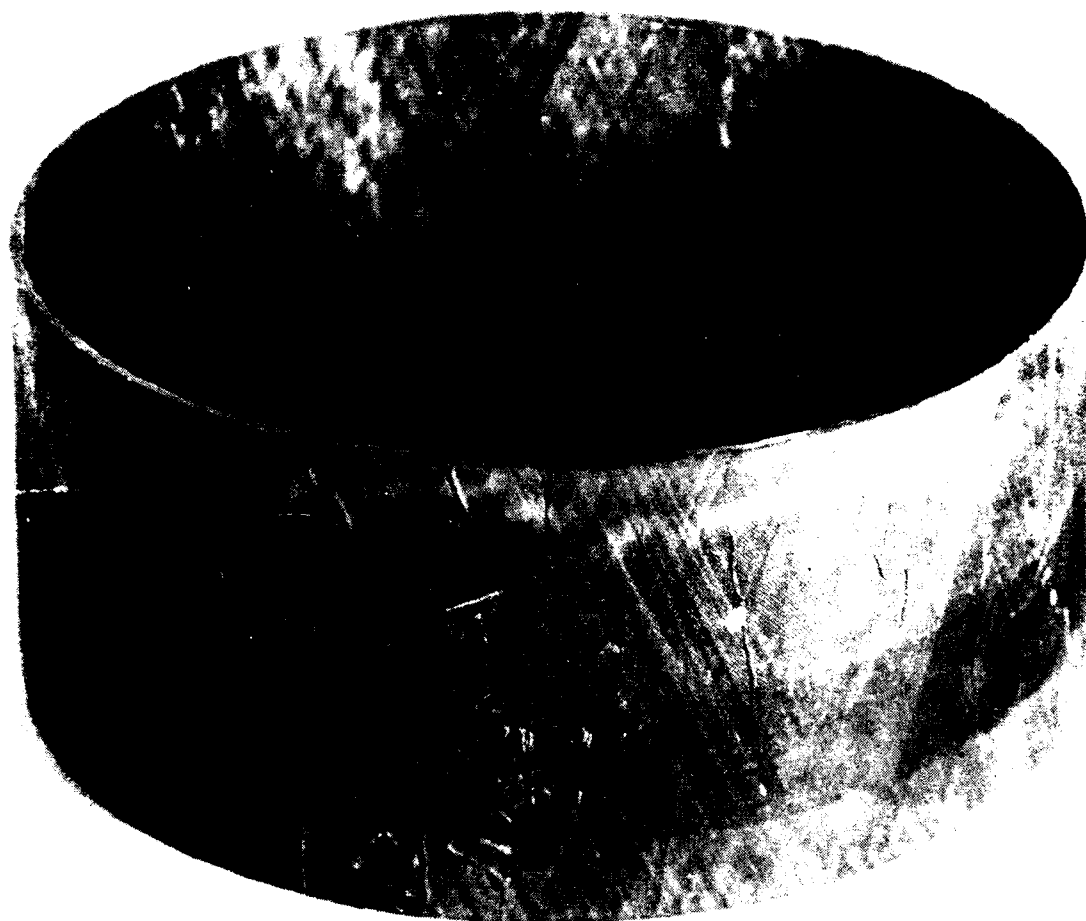


Figure 1. The cylindrical container used in the experiment.

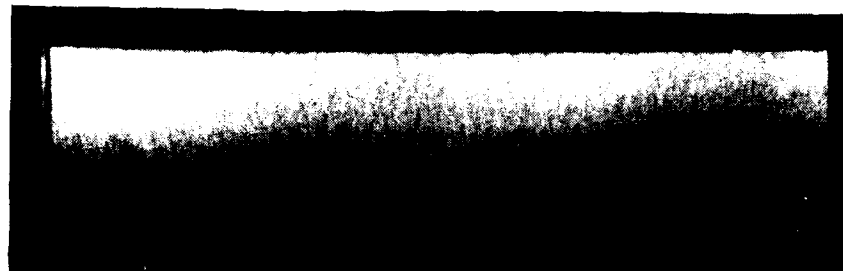
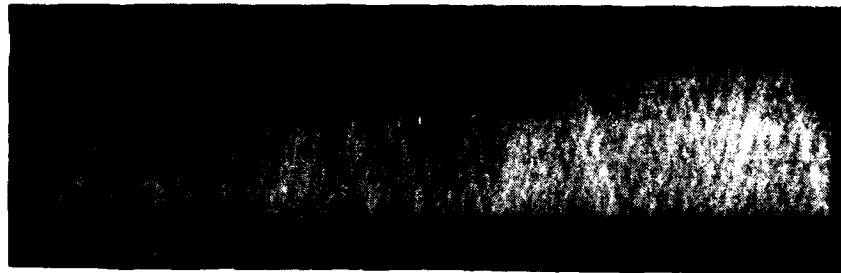


Figure 4. Radial geometry scans of AFAL Sample 1, top scan on OD, bottom scan at nominal ID. Compare to Figure 5.

sented as if unwrapped and laid flat. (A paper clip affixed to the cylinder gives a rotational angle reference point.)

Figure 5 shows the same two slices scanned tangentially. It is clear that the tangential geometry gives better sharpness and contrast. The fiber pattern is clearly shown near the surface, and we believe its contrast relative to the rest of the structure is related to density differences. The broad, dark to light shadings in the images are probably related to cylinder radius variations.

AFAL Sample 2. Six (6) radial geometry scans were made of this object at 0.05 in. increments using the Type B collimator. (Only one end of the 8 in. long cylinder was scanned.) Two of the scans, taken at the outer surface (R_0) and nominally at mid-wall ($R_0 - 0.10$) are shown in Figure 6. Fold-like surface features on the cylinder are clearly seen on the first photograph, along with a hint of the chevron-shaped pattern of the fibers. One of the folds (right-center) was visually observed to extend partway into the wall on one end of the cylinder. The second photograph shows that this fold extends only 2.5 in. or 3 in. in from the cylinder end. (The image height covers about 4 in. of cylinder.) Other folds or wrinkles appear to be only near the surface and are not evident in the lower photograph.

AFAL Sample 3. Several linear scans were made of this object, but they showed no detail of interest and were not photographed. This object had a wall thickness significantly less than the ZT slice thickness, and the only structure visually observed was very fine, i.e., much smaller than our ZT resolution.

AFAL Sample 4. Figure 7 is a photograph of this sample. It was the only object that we scanned with both Type B and Type C collimators. Both radial and tangential geometry scans were done with the Type B collimator, and as for the 8 in. cylinder discussed above, the tangential scans gave sharper images of the generally circumferential defects seen in Figure 7.

Figure 8 is a sequence of the eight (8) tangential scans. Their locations relative to the outside radius R_0 are shown on the caption. These images have

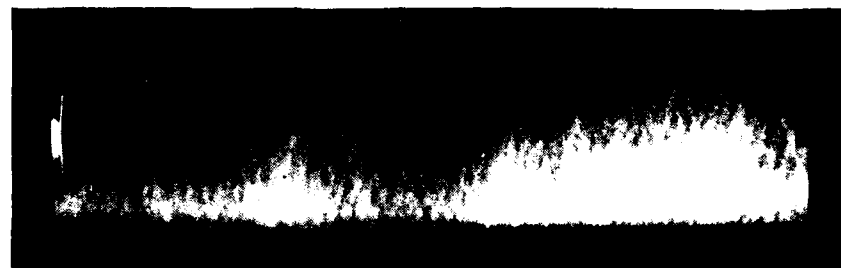


Figure 5. Tangential geometry scans of AFAX Sample 1, top scan focussed on OD.
bottom scan at nominal ID. Compare to Figure 4.

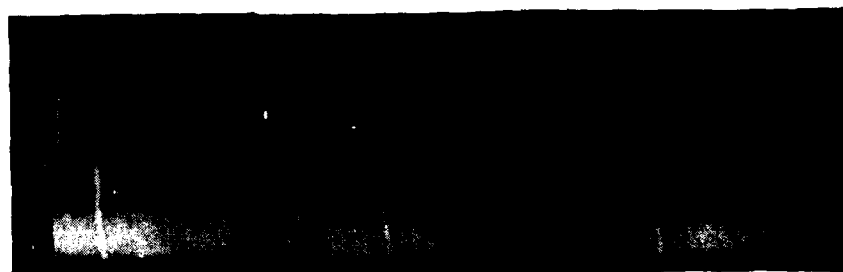


Figure 6. Radial geometry scans of AFAL Sample 2, focussed on outer surface
(top) and mid-wall (bottom).

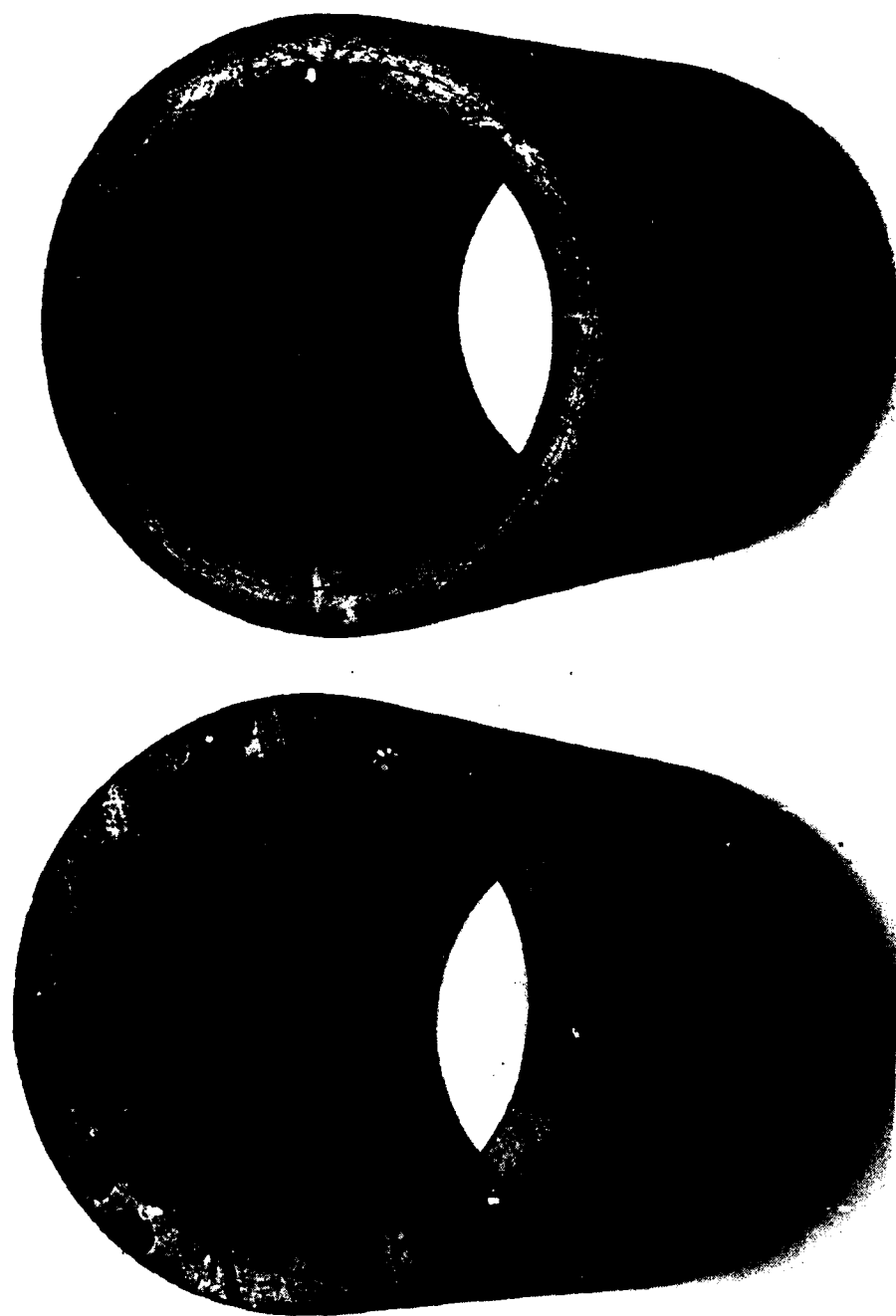


Figure 7. AFAL Sample 4 (refer to Table 2). Delamination flaws, visible at both ends, extend along the entire sample.

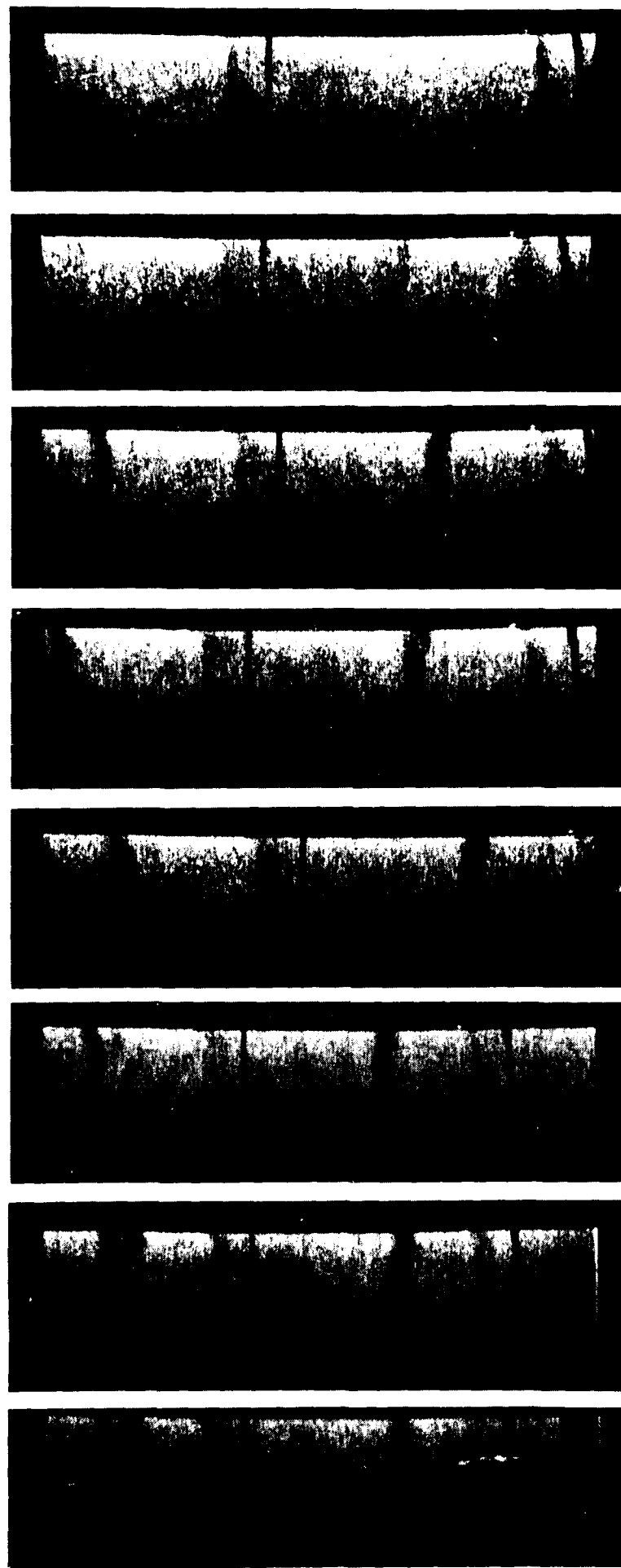


Figure 8. A sequence of 8 transgential geometry scans of AFM Sample 4. The positions of the scans relative to the outer radius R_0 of the sample are R_0 : 0.338, 0.385, 0.435, 0.440, 0.445, 0.450, 0.485, and 0.500 inches, shown from top to bottom, respectively.

angular fiducial marks in the form of two lengths of solder (one long, the other short). Furthermore, the solder shadows the detector during part of the rotation cycle, producing a reduced signal during that time. These shadows are observable to the left of the black bars produced when the solder blocks the primary beam. Neither the solder bars nor their shadows are real features of the sample. The structure shown in the defects themselves, as a function of slice radius, is real. For example, the "Y" shaped defect near the top of the cylinder can be confirmed visually.

Because of focal length of the new Type C collimator (3.0 in.) is less than the radius of the turntable used to rotate the samples, a true tangential scan could not be done. Instead, the scans were taken at about 45 in., i.e., at a geometry roughly midway between those shown in Figure 2.

Figure 9 compares the same region of the sample as scanned with the Type B, tangential and Type C, 45° scans. These photographs also demonstrate the effectiveness of the slower sweep speed at reducing afterglow artifacts. Close observation of the background noise shows it to be characterized by vertical streaks in the Type B scans, whereas these are much reduced in the Type C scan. The vertical corresponds to the direction of chopper wheel motion and is the direction in which afterglow artifacts are manifested.

Phantom Studies

Four types of phantoms were constructed to investigate the prototype ZT system's performance with regard to delamination, porosities, density fluctuations and chemical species variation. The phantoms, described in Section 1.3, are generally as described in the Phase I contract SOW (see Appendix B).

All the phantom studies were performed using the improved, Type C collimator and sampling scheme. They were all flat-plate phantoms, so the linear scan geometry was employed. Before proceeding, a support fixture was prepared to hold the phantoms with their faces precisely parallel to the translation stage motion. Except as noted, scans were done at 90 kV and 10 mA as X-ray tube operating conditions. Limited experiments were done at different kilovoltages.



Figure 9. A tangential scan of AFAL Sample 4 (top) done with the Type B collimation/sampling system, compared with an approximately radial geometry scan (bottom) done with the Type C system. The delaminations are better seen in the upper image because of the tangential geometry. The quality of the noise background is much improved in the lower image, however, because the afterglow effects have been eliminated.

ranging from 75 kV to 100 kV, with no apparent effect on results except as related to photon statistics, and therefore to S/N ratio. Low kilovoltages give considerably less X-ray flux, and the X-ray tube was unstable above about 90 kV.

The phantom images were examined by at least three observers (PJB, RDS, and/or RS and EH). There was general agreement about the limiting detectability of the defects, so blind studies were not required.

Delamination Phantom

For scans of the delamination phantom, the slice plane was positioned to coincide with the face of the cavities representing delaminations. Scans were made with various overlying thicknesses of the same material (Delrin, density 1.47 gm/cm^3). Figure 10 is a representative image, showing the delamination phantom with 1/2 in. of overlying Delrin. There is agreement that the 5th cavity of depth 0.005 in. (1/8 mm) can be observed in this image. Full results are tabulated and interpreted in the section covering phantom image analysis.

Porosity Phantom

Positioning and scanning of this phantom was similar to that for the delamination phantom. A representative image, Figure 11, shows the porosity phantom with 1/2 in. of overlying Delrin. In this image, the 6 largest holes of the 9 can be detected in rows 1 and 2, and 5 holes in rows 3 and 4. See the section on phantom image analysis.

Density Phantom

It had originally been our intent to construct a density phantom consisting of aqueous solutions of sucrose, encapsulated in a Delrin base structure. The proportions of sucrose and water (H_2O) can, in principle, be adjusted to match a density of 1.47 g/cm^3 and to achieve density variations around that value in accordance with the criteria in the SOW. In practice, however, this proved to

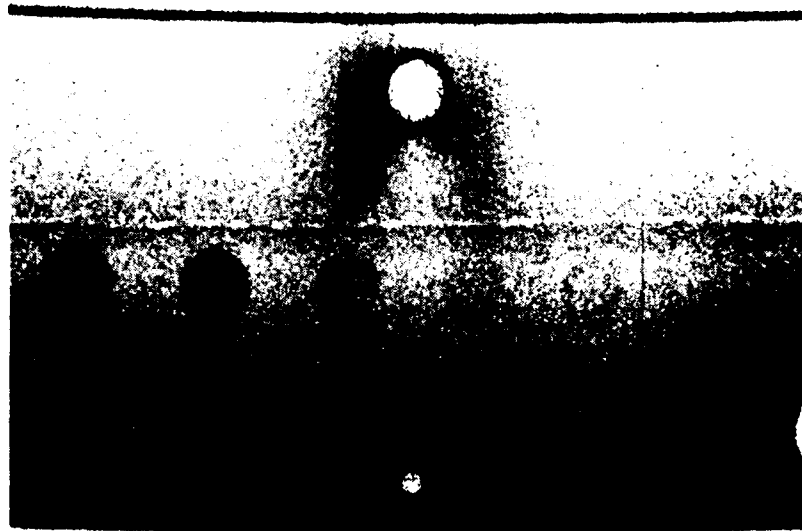


Figure 10. The delamination phantom scanned through 0.5 in. of overlying Delrin. From left-to-right, the delamination depths are 0.080, 0.040, 0.020, 0.010, 0.005, and 0.0025 in. The last cannot be seen in this image. The 0.005 in. delamination appears as an annular ring, which it in fact was because of a manufacturing error.

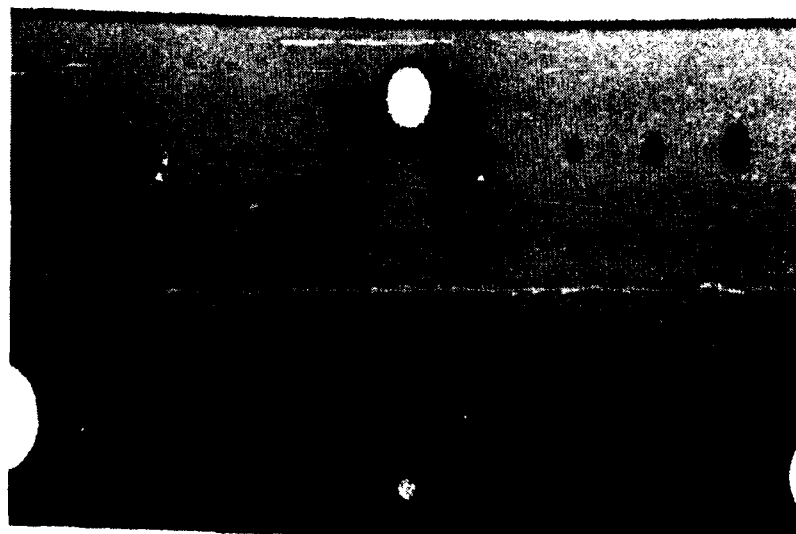


Figure 11. The porosity phantom scanned behind 1/2 in. of overlying Delrin.
Six pores can be seen in the upper two rows and five in the lower
rows.

be impractical, a new base structure of Lexan, density 1.24 gm/cm^3 , was constructed, for which the sucrose aqueous solutions could be matched.

Another problem occurred, however. The sucrose solution cells in the Lexan were encompassed in dark rings in the ZT images (see Figure 12) which we believe were related to some unexpected chemical change in the Lexan, possibly as a result of the cement used in fabrication of the phantom. They made the phantom unusable, so we were forced to try yet another density phantom design.

The final density phantom did not require the use of cements, and although it has a different mechanical configuration than originally planned, it is useful to evaluate sensitivity to density variations. The base material is acrylic. Corresponding sucrose/water solutions were made. Chemically, the acrylic and sucrose solutions are not greatly different, although the sucrose solution density could be finely adjusted. The smallest density difference which could be clearly resolved was about 2%. Figure 13 is a ZT image of this phantom for one of the sucrose fills that were used. Other mixtures with a different range were also scanned.

Chemistry Phantom

The chemistry phantom also had to be constructed from Lexan in order to be able to achieve aqueous solution densities matching the base structure. The mechanical configuration was as originally planned, however. From left to right, the cells were filled with sucrose, ZnCl_2 , KI , and CaCl_2 , all mixed to a density of 1.21 gm/cm^3 , closely matching the 1.24 gm/cm^3 of the Lexan. The two right-most cells were empty.

Figure 14 is a scan of the phantom along the front boundary of the cells. Although the densities in this case are all the same, it is obvious that the situation is far different than it was for the sucrose-based density phantom. The sucrose within the left-hand cell is chemically similar to the Lexan, and therefore contrasts little or not at all with it. The CaCl_2 and ZnCl_2 , in that order, have higher atomic number constituents, resulting in proportionately



Figure 12. A scan of the original density phantom with low contrast mixtures of sucrose in each of its six cavities. This phantom was unusable because the dark rings (possibly due to the cement used in fabrication) and the air bubbles could not be eliminated. The total range of sucrose densities in this image is 0% to 3% relative to the base material.

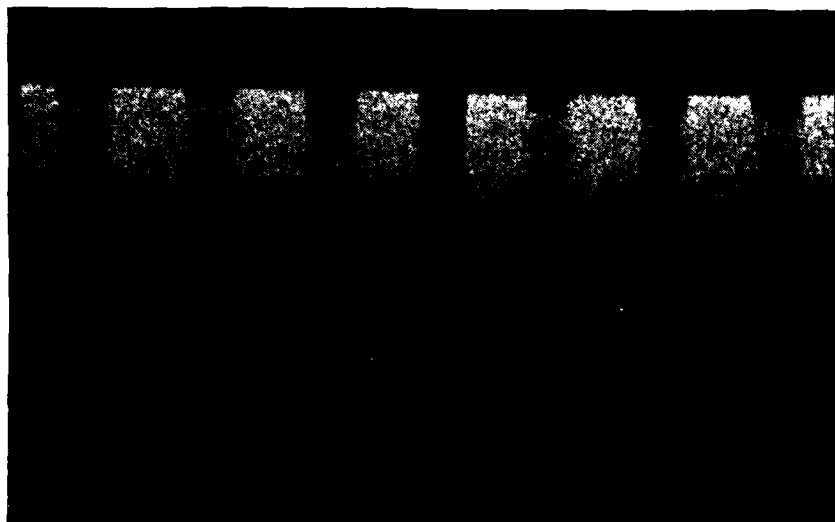


Figure 13. The replacement density phantom, fabricated of acrylic and having sucrose solution fills of calculated densities 1.167, 1.159, 1.150, 1.00 (H₂O), and 1.154 gm/cm³ for the first 5 cells (left-to-right); the last 2 cells have been calibrated. The first and third cells differ in density by about 1.5%, for example.

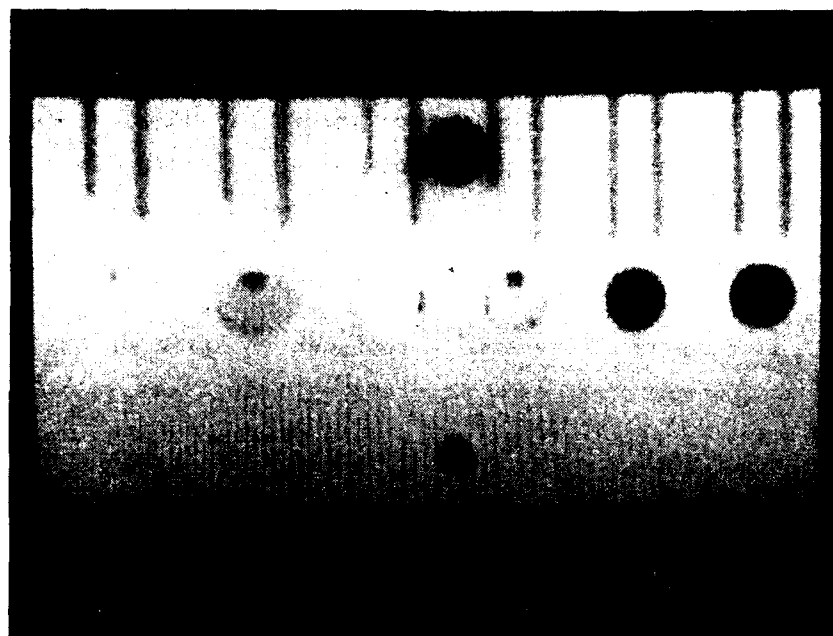


Figure 14. A scan of the chemistry phantom, slice-centered on the boundary between sample cell and the overlying cover plate. From left-to-right, the four filled cells (the two on the right were empty) have aqueous solutions of sucrose, ZnCl, KI and CdI₂, all mixed to a density of 1.21 cm/cm³ to match the substrate. The KI cell "lights up" in fluorescent radiation from the iodine constituent.

more photoelectric absorption of the X-rays and less Compton scattering; they are therefore less bright in the ZT scattered image.

We had expected a similar effect for the KI, but even more strongly. Contrary to expectation, it gave a very strong ZT signal. This is evidently the result of fluorescence of the iodine which produces fluorescece X-rays of energy (near 30 keV) sufficiently high to exit the phantom with relatively low attenuation.

Although we have not attempted a thorough analysis of the chemical sensitivity of the ZT technique, some interesting things can obviously occur. We believe there may be applications where this chemical discrimination (independently of density) will be of interest.

Results for Phantom Images

The data from the delamination and porosity phantoms are analyzed in this section. In each case the observers reviewed images of the phantoms with differing overlaying material and determined which of the defects were visible and which were not visible. Image manipulation in the form of contrast enhancement was used. It is felt that this was allowable because it is our intent that any Phase II system proposed would have this feature. If there was question about the visibility of any given defect, the image was masked to allow visualization of the area of the defect only. This prevented obtaining visual clues from other areas of the image. As an example, the delaminations in the delamination phantom are equally spaced and in one row. The spacing can become a clue as to where to expect to see the next delamination. However when the other defects are blocked off, the observer cannot utilize the symmetries of the phantom to improve detection capability.

The results of this study are given in Tables 3 and 4. In each case the phantom was studied with varying amounts of materials overlaying the defects. For the defect phantom if the defect was visible it is indicated with a 'Y'. If it is not visible it is indicated with a 'N'. If the defect is only par-

tially visible or if it was felt that it was at the threshold of detection, it is indicated with a 'T'.

For the porosity phantom, the number of holes visible in each row is indicated. If there was any question about the detectability of the last visible hole in a row, it is indicated by listing two values. An entry 6/7 means that six holes are clearly visible and the seventh is at the threshold of detection.

The results are as expected. For any given defect, the probability of detection decreases as the amount of overlaying material increases and as the size of the defect decreases. The correlation with the amount of overlaying material is probably related to the observed X-ray flux in the image. As the overlaying material increases, the number of X-rays reaching the plane of the defect decreases, decreasing the detected scatter and increasing the quantum noise in the image. The correlation with the size of the defect is probably related to the contrast of the defect in the image.

Table 1: SCAN PARAMETERS

A. All Scans

. X-Ray technique factors:	90 kV, 10 mA
. Source-slit distance:	24.5 in., nominal
. Slit width:	0.040 in. (1 mm)
. Source-chopper distance:	14.5 in., nominal
. Chopper slits:	0.040 in. (1 mm)
. Scanned height (at ZT focus):	4 in., nominal
. Image matrix:	512 x 512 pixels

B. Initial Collimator Design

. Collimator thickness:	5.5 in.
. Focal length:	5.5 in.
. Slice thickness:	0.150 in. FWHM
. Pixel volume (nominal):	3.75 mm ³
. Solid angle detected:	(TBD)
. Scanning rate:	240 sweeps/sec
. Sweeps added:	396
. Total scan time:	14 min, 4.8 sec
. Pixel integration time:	3.22 msec

C. Improved Collimator Design

. Collimator thickness:	3.0 in.
. Focal length:	3.0 in.
. Slice thickness:	0.120 FWHM
. Pixel volume (nominal):	3.0 mm ³
. Solid angle detected:	(TBD)
. Scanning rate:	16 sweeps/sec
. Sweeps added:	16
. Total scan time:	8 min, 32 sec
. Pixel integration time:	1.95 msec

Table 2: AFAL-SUPPLIED SAMPLE

Sample 1 (Figure 3)

- . Description: Wound, carbon-fiber cylinder with no visible defects, but with slight variations in diameter (i.e., out-of-roundness)
- . Diameter: 8 in. OD, nominal
- . Wall thickness: 0.09 in.
- . Length: 3.5 in.

Sample 2

- . Description: Carbon-fiber cylinder with what appeared to be folds in the layers that extended outside the nominal radius and partly through the wall.
- . Diameter: 5 in. OD, nominal
- . Wall thickness: 0.20 in.
- . Length: 8 in.

Sample 3

- . Description: Layered sheet, approximately 15 in. by 11 in. with 1/16 in. wall thickness and slightly bowed in the longest dimension with a radius of curvature of about 3 feet. (Accurate dimensions not recorded.)

Sample 4 (Figure 7)

- . Description: Graphite-epoxy cylinder with noticeable internal delaminations.
- . Diameter: 5.25 in.
- . Wall thickness: 0.63 in.
- . Length: 8.25 in.

TABLE 3

DEFECT THICKNESS (INCHES)

AMOUNT OF OVERLAYING MATERIAL (IN.)	0.080	0.040	0.020	0.010	0.005	0.0025
0.125	Y	Y	Y	Y	Y	*
0.250	Y	Y	Y	Y	Y	*
0.500	Y	Y	Y	Y	Y	N
1.000	Y	Y	Y	T	N	N
1.500	Y	Y	T	N	N	N
2.000	Y	N	N	N	N	N

* This defect may be visible in this image. However, the construction was such that the defect was an annular ring rather than a disk. The detection was considered questionable because the whole disk was not seen. However, later review of the physical phantom showed the manufacturing to be consistent with the image.

TABLE 4

NUMBER OF HOLES VISIBLE IN A ROW

AMOUNT OF OVERLAYING MATERIAL (IN.)	ROW 1	2	3	4
0.125	7	7	6	5
0.250	6/7	6/7	5	6
0.500	6/7	6	5	5
1.000	6	5	4/5	5
1.500	4	3/4	2/3	3
2.000	2/3	1	0/1	0/1

THEORETICAL ANALYSIS OF RESULTS

Data Analysis

The data described in the previous section must be used to attempt to understand the backscatter phenomenon in sufficient detail to allow accurate extrapolation of the results as system parameters change. In particular, we would like to be able to accurately predict the performance of the system that is proposed for the Phase II program. To this end we have developed a theoretical model of the total system, including the backscatter process and the human detection probability, and compared this model to the results of the phantom studies, and will use this model to predict performance of the Phase II system.

The model includes two parts; the physics of the experimental set up and the interaction of a human with the imaging system. We will consider the human interaction first. The probability of detection of a signal in a noisy background has been considered by many investigators. They have agreed on a mathematical description that well describes experimentation and allows one to predict when an observer will detect a signal in a noisy background. The variable which differentiates detection is called the signal to noise ratio and abbreviated S/N. Basically most experimenters agree that when the signal to noise ratio exceeds 5 for a system, most observers will agree that the signal is seen. Below this level there will be disagreement and eventually lack of detection and above this level there always will be detection.

What we have done is to construct a simple model of the experiments which lets us predict a S/N ratio for the various experimental configurations. This model is then compared to the experimental results. In a well built X-ray system, the statistical fluctuation in the number of detected photons (called quantum noise) in the image is the dominant source of noise. The other potential source of noise, due to electronic noise in the preamps or processing electronics, is far smaller than the quantum noise.

We assume, therefore, the noise in the image is related to the quantum noise in the detected photons. The number of detected photons will be equal to:

1. The number of photons incident on the phantom times
2. The transmission of the phantom material that is between the source and the slice to be imaged times
3. The probability of backscatter in the slice times
4. A geometric factor times
5. The transmission of the phantom material between the slice and the backscatter detectors times a factor relating to the probability of detection.

This is discussed in detail in Appendix A. Here we present a very simplified version relating to these specific phantoms only. In the data utilizing the delamination phantom and the porosity phantom the only variables were the amount of phantom materials overlaying the slice and the probability of scatter in the slice. Therefore to understand these data our model will only have these two factors as variables.

We will assume that there are F_0 photons/pixel incident on the phantom and that the transmission of the phantom material per unit length is T , the thickness of overlay material is t , and that the probability of scatter in the plane is P and that the detection efficiency is E . Then the number of detected photons per pixel will be approximately:

$$F_d = F_0 (T)^t P (T)^t E \quad (1)$$

where we have assumed that the distance in and out of the material is the same. This is a simplifying assumption. This is just an algebraic expression of the physical processes discussed above. Since t and P are the only variables in our experiments, this may be rewritten more simply:

$$F_d = k P (T)^{2t} \text{ (photons/pixel)} \quad (2)$$

where k is the product of all the other factors. This is the flux per pixel. So to determine the flux seen over a defect it must be multiplied by the area of the defect, A :

$$F = k P (T)^{2t} A \text{ (photons/defect)} \quad (3)$$

The signal one is attempting to detect, S , then is the difference in the detected flux in the area of the defect (F_2) and a neighboring area of similar size (F_1) without a defect.

$$S = F_1 - F_2 \quad (4)$$

The noise is the square root of the number of detected photons in the region without a defect.

$$N = (F_1)^{1/2} \quad (5)$$

Therefore, the signal to noise ratio for the defect detection is:

$$S/N = k (T)^{2t} A (P_1 - P_2) / (k (T)^{2t} A P_1)^{1/2} \quad (6)$$

where P_1 is the probability of scatter in Region 1 and P_2 is the probability of scatter in Region 2. Or:

$$S/N = k^{1/2} (T)^t A^{1/2} [(P_1 - P_2) / P_1^{1/2}] \quad (7)$$

Now the signal to noise ratio is expressed in terms relating to the phantom experiment if one can evaluate the last expression. To estimate the term in brackets we let the P 's equal the normalized amount of phantom material in the slice. That is, if there is no defect in the pixel of interest in the slice plane, the $P = 1$. If the defect is large enough so that there is no phantom material in the slice plane, then $P = 0$. If the slice plane is half filled then $P = 0.5$. It is important to note that if the defect size is less than the size of the X-ray beam at the slice plane (i.e., the defect is smaller than a

pixel), then P is correctly calculated as the percentage of the voxel (volume element) that is filled with material.

Comparison of Model with Results

Now we have constructed a model where we can predict the S/N ratio for each defect in the delamination and defect phantoms. This model has only two free parameters, k and T. All other parameters are known. Remembering that it takes a S/N ratio of 5 or more to detect a given defect, one can construct a set of inequalities from the observations of Tables 3 and 4. Unfortunately one does not know the exact value of the S/N ratio for each observation; one can only say whether it is greater than or less than 5. To be able to use these data to obtain quantitative values for the constants we took the average value of the S/N for the last visible defect and the first non-visible defect and set that to 5. This is an approximation but Tables 3 and 4 provide 28 independent measurements. The values of S/N that were obtained with the same amount of overlaying materials (for both phantoms) were then averaged together. This then yields 6 numbers that are a function of k and T and vary with the amount of overlaying material, t. A least squares fit was made to these data to obtain the final model for S/N:

$$S/N = 437. (0.284)^t A^{1/2} (1-P_2) \quad (8)$$

This model can then be used to predict the signal to noise ratios of each of the phantom measurements and one can compare the S/N ratios with the detectability of each defect. Tables 5 and 6 are repeats of Tables 3 and 4 except that the predicted S/N ratio for each phantom defect is noted in parentheses. The agreement with theory is excellent and therefore this model may be used to predict the performance of a Phase II system.

TABLE 5

DEFECT THICKNESS (IN.)

Observed and Theoretically Predicted (in parentheses)
Visibility of Delamination Defects

AMOUNT OF OVER- LAYING MATERIAL	0.080	0.040	0.020	0.010	0.005	0.0025
0.125	Y(Y)	Y(Y)	Y(Y)	Y(Y)	Y(Y)	*(Y)
0.250	Y(Y)	Y(Y)	Y(Y)	Y(Y)	Y(Y)	*(N)
0.500	Y(Y)	Y(Y)	Y(Y)	Y(Y)	Y(T)	N(N)
1.000	Y(Y)	Y(Y)	Y(Y)	T(T)	N(N)	N(N)
1.500	Y(Y)	Y(Y)	T(T)	N(N)	N(N)	N(N)
2.000	Y(Y)	N(Y)	N(N)	N(N)	N(N)	N(N)

* This defect may be visible in this image. However, the construction was such that the defect was an annular ring rather than a disk. The detection was considered questionable because the whole disk was not seen. However, later review of the physical phantom showed the manufacturing to be consistent with the image.

TABLE 6

NUMBER OF HOLES VISIBLE IN A ROW

Number Observed and Number Theoretically Predicted (in parenthesis)
of Holes in the Porosity Phantom

AMOUNT OF OVERLAYING MATERIAL (IN.)	ROW	1	2	3	4
0.125		7(7)	7(7)	6(6)	5(6)
0.250		6/7(7)	6/7(7)	5(5)	6(6)
0.500		6/7(7)	6(7)	5(5)	5(5)
1.000		6(6)	5(6)	4/5(3)	5(4)
1.500		4(4)	3/4(4)	2/3(1)	3(3)
2.000		2/3(2)	1(2)	0/1(0)	0/1(2)

CONCEPTUAL PHASE II STUDY

Beam Modulator

The test setup used had several limitations which directly impacted image quality. First, the distance from the X-ray focal spot to the collimator focal line was fixed at 26.375 in. This did not allow for use of all of the flux generated by the X-ray tube. Had all the available flux been used, the time required per scan could have been reduced substantially, or for a given scan time the image resolution would have been superior. Second, the distance from one of the pencil beam defining apertures to the ZT collimator focal line was a fixed 13 in. This had the effect of reducing the spatial resolution of the system in the vertical direction. Neither of these dimensions are in any way fundamentally fixed, however, they do reflect the limitations of a the chopper wheel beam definer system used.

A design study was conducted to determine the feasibility of reducing both of these dimensions, thereby increasing both flux and spatial resolution, as much as possible. The concept was to design a beam definer that could fit between the two halves of the ZT collimator/detectors. After looking at several possible geometries, a design based on a reciprocating ball reverser was chosen. This design is shown in Figure 15. The ball reverser is similar to a ball screw except that its machined thread reverses itself at the end of its stroke, thus converting rotary motion to linear reciprocating motion.

A detailed layout of this design is shown in Figure 16. The X-ray source is enclosed in a lead lined box to ensure no radiation leakage from the source is picked up by the ZT detectors. The source is positioned and its housing designed to allow it to be as close as possible to the test article (12.750 in. vs. 26.375 in. in the test system). By doing so, the X-ray flux striking the test article would be over four times what was available in the test system. The net result will be to allow scans with the same image quality to be taken in one-fourth the time or to obtain images with twice the defect sensitivity.

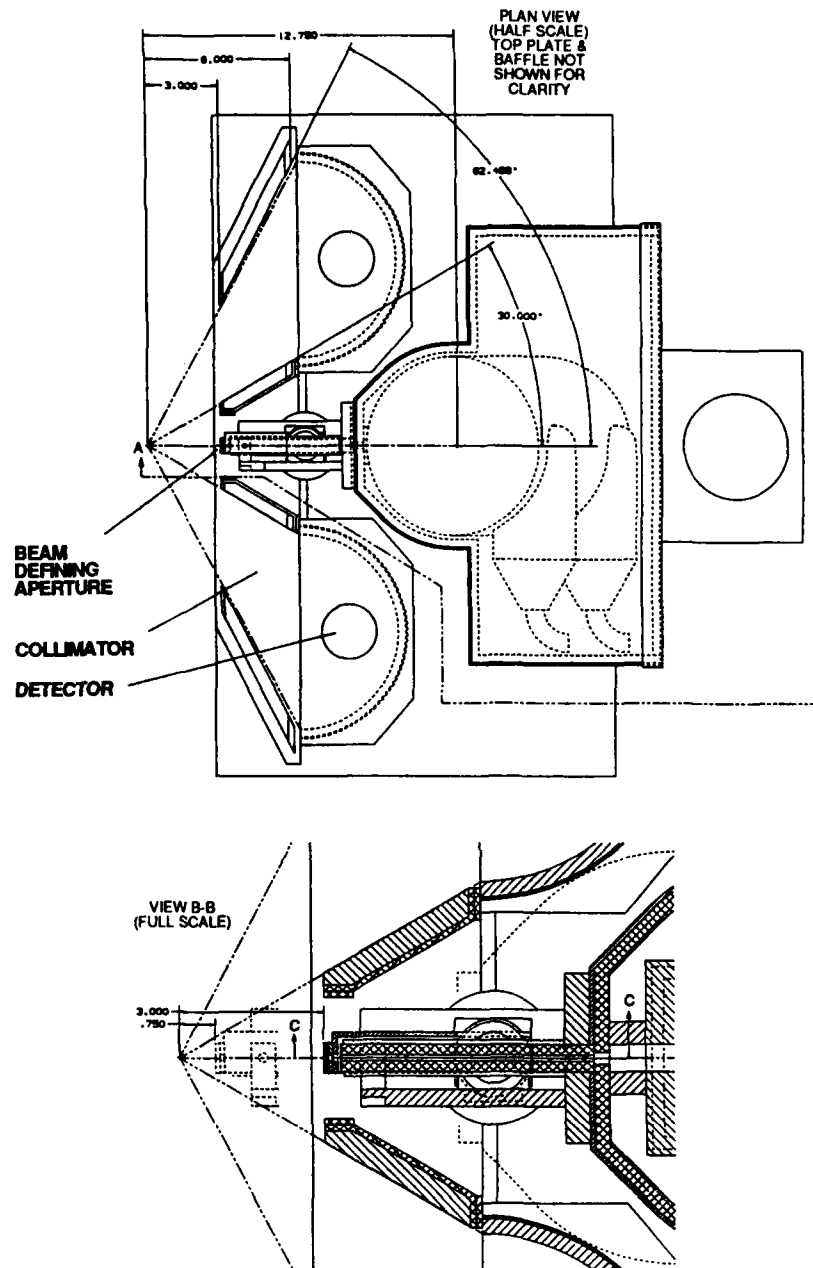


Figure 15. Conceptual design for a Phase II system. Of particular interest here is the location of the beam modulator between the two backscatter detectors. This positively affects the sensitivity and spatial resolution of the system. View B-B shows in phantom lines how the modulator can be moved forward of the front surface of the collimator for inspection of thin walled objects. This allows a further increase in available X-ray flux.

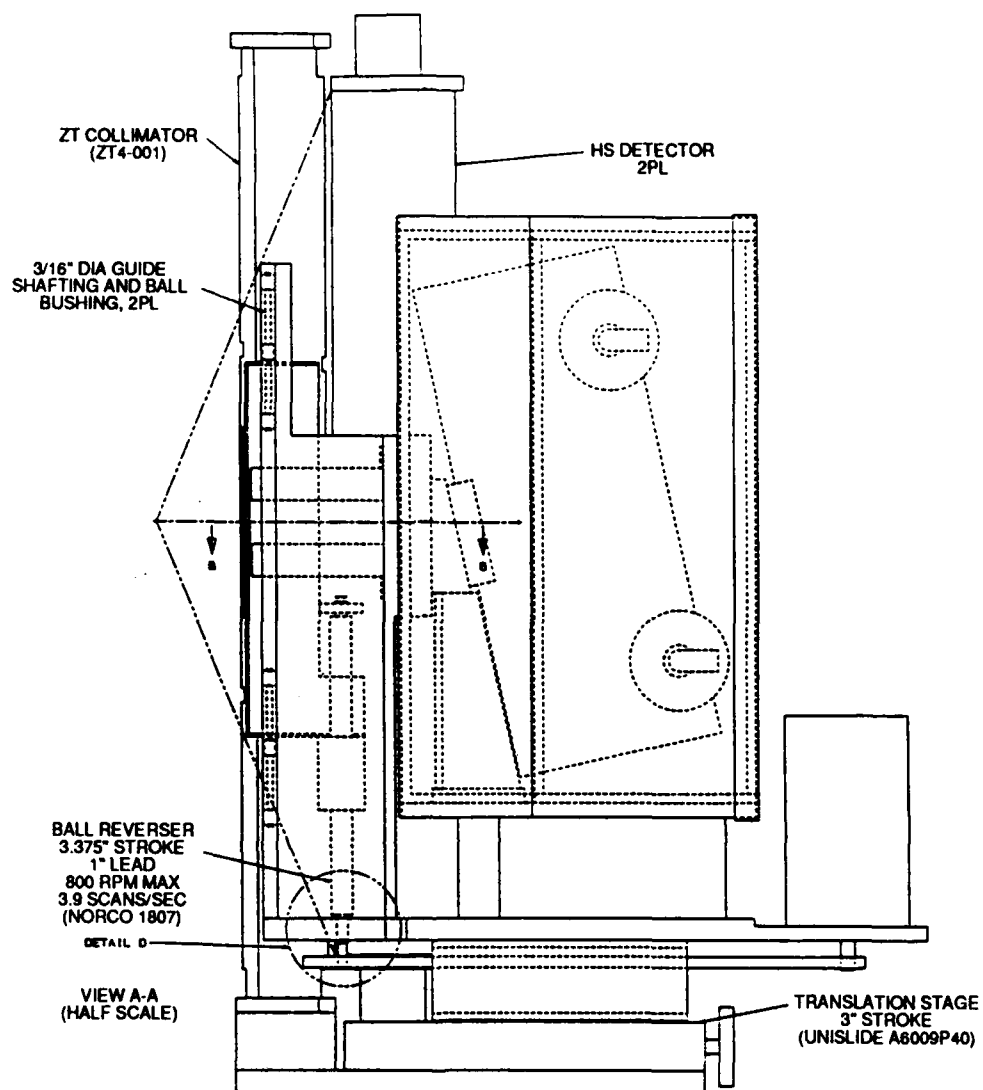


Figure 16. Side view of the proposed Phase II system. It shows the relationship of the X-ray tube collimator and detectors. The dashed lines show the very large angular acceptance of the backscatter detectors.

The pencil beam aperture consists of two pairs of tungsten jaws, one pair with a horizontal slit and one pair a vertical slit, driven by the ball reverser. These reciprocating apertures, the X-ray source and its housing are mounted on a translation stage. This stage allows the entire assembly to be moved forward as close as possible to the test object, which will result in an image with maximum spatial resolution.

The other design options studied for generating the moving pencil beam included a slider crank driven reciprocator, a rotating hoop with multiple holes, a series of small synchronized chopper wheels, and a voice coil driven reciprocator which rides on air bearings. All of these would have allowed for the same gains in X-ray flux and spatial resolution as the ball reverser design concept. The ball reverser, chosen because it provided for the simplest design, is limited to approximately four pencil beam scans per second. Preliminary studies have shown that this will be fast enough. However, if further evaluation shows that a higher scan rate is more appropriate, one of the other concepts could be used.

Phase II System Description

There are two main criteria in coming up with a concept for a Phase II system. First, and foremost, is image quality. The main goal of all X-ray systems that AS&E produces is to obtain the best image possible. Second is flexibility in use. A laboratory based system should be designed so as to be able to inspect a variety of different shapes, sizes and thicknesses of test objects at various incident beam angles.

Mechanical Hardware

A mechanical hardware concept for the Phase II system which meets these two requirements is shown in Figures 17, 18 and 19. The system shown can be broken down into three main assemblies; the source housing and pencil beam modulator, the ZT collimator/detectors and transmission detector, and the test article manipulating equipment. The source housing and beam modulator will be designed along the lines of the hardware described in the previous section.

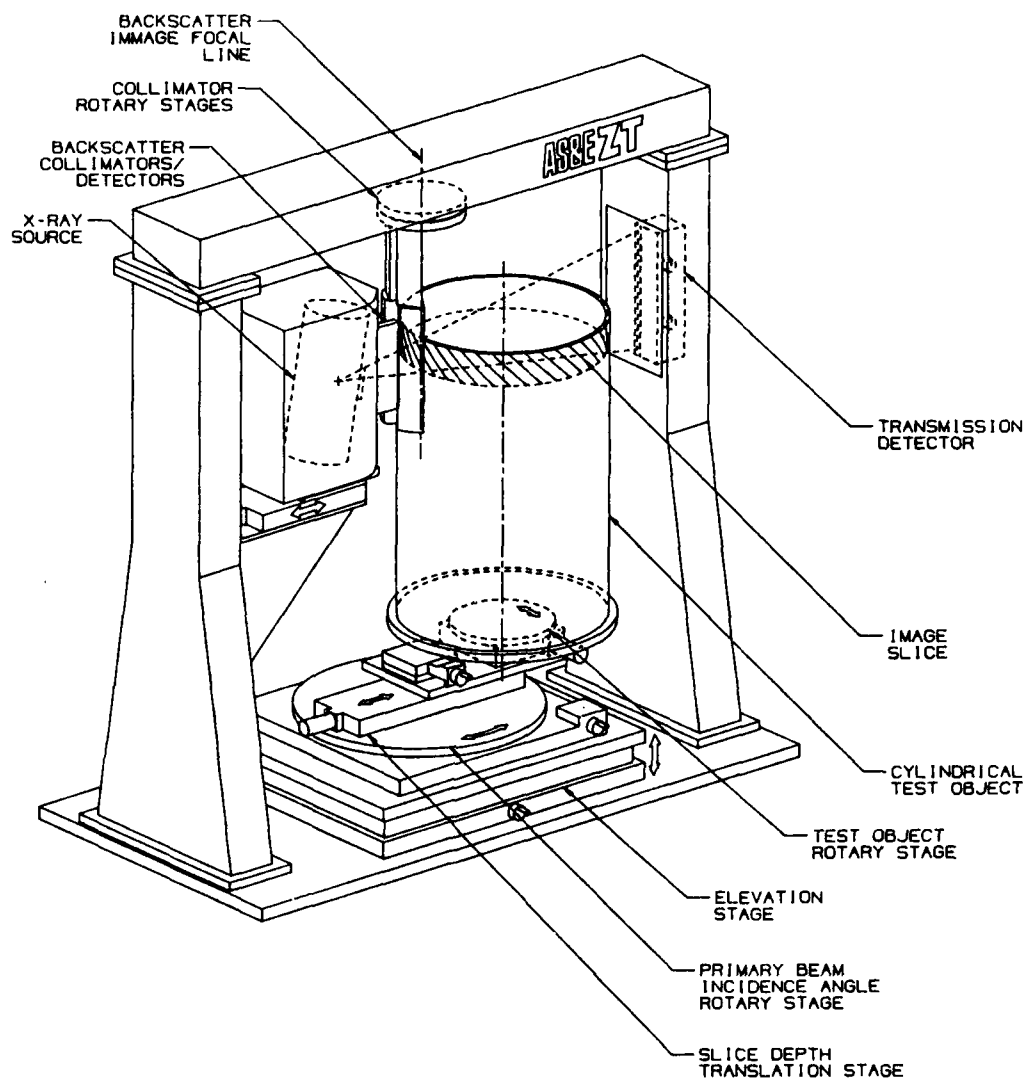


Figure 17. Phase II System Mechanical Hardware with Cylindrical Test Object.

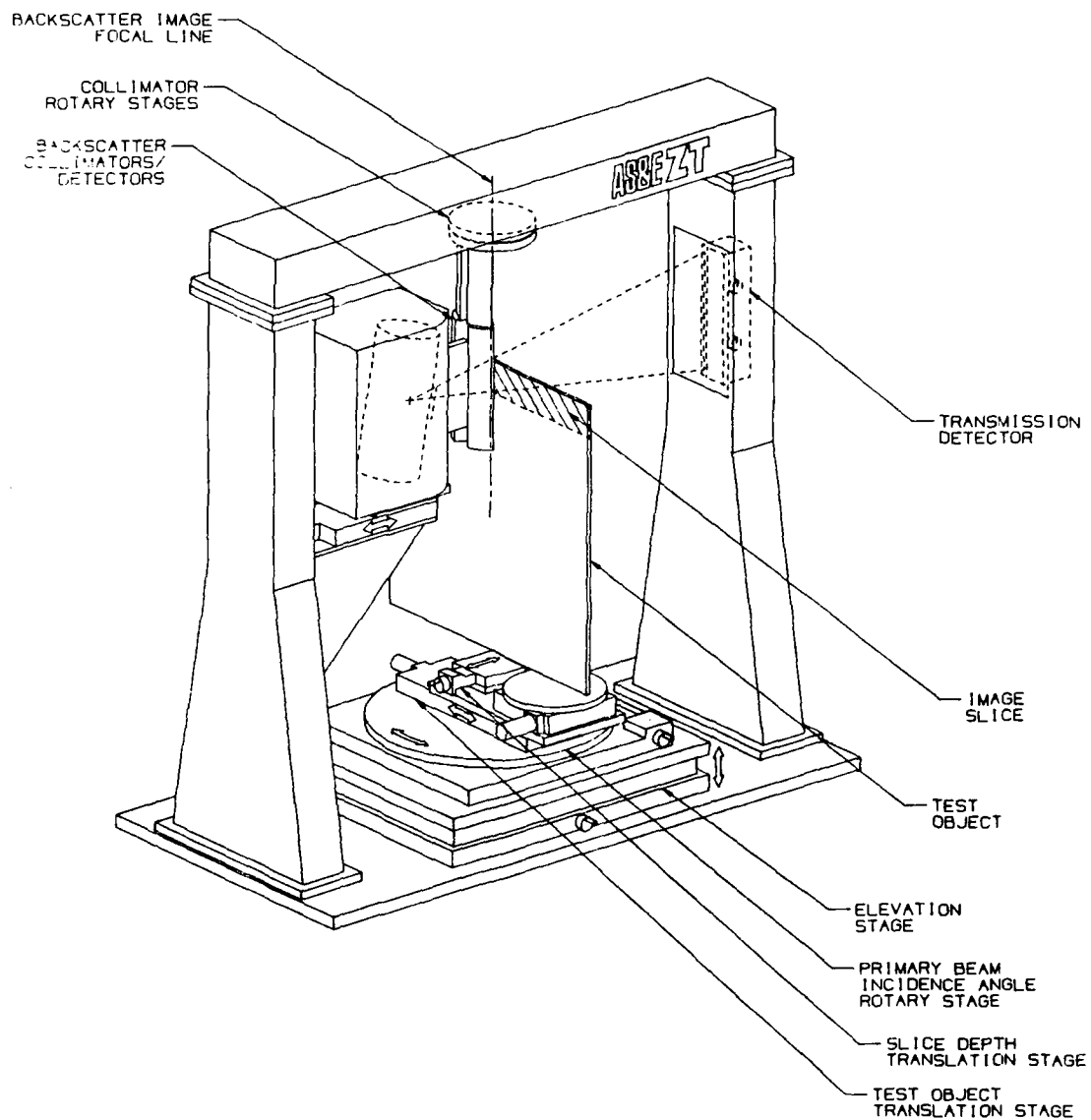


Figure 18. Phase II System Mechanical Hardware with Flat Test Object.

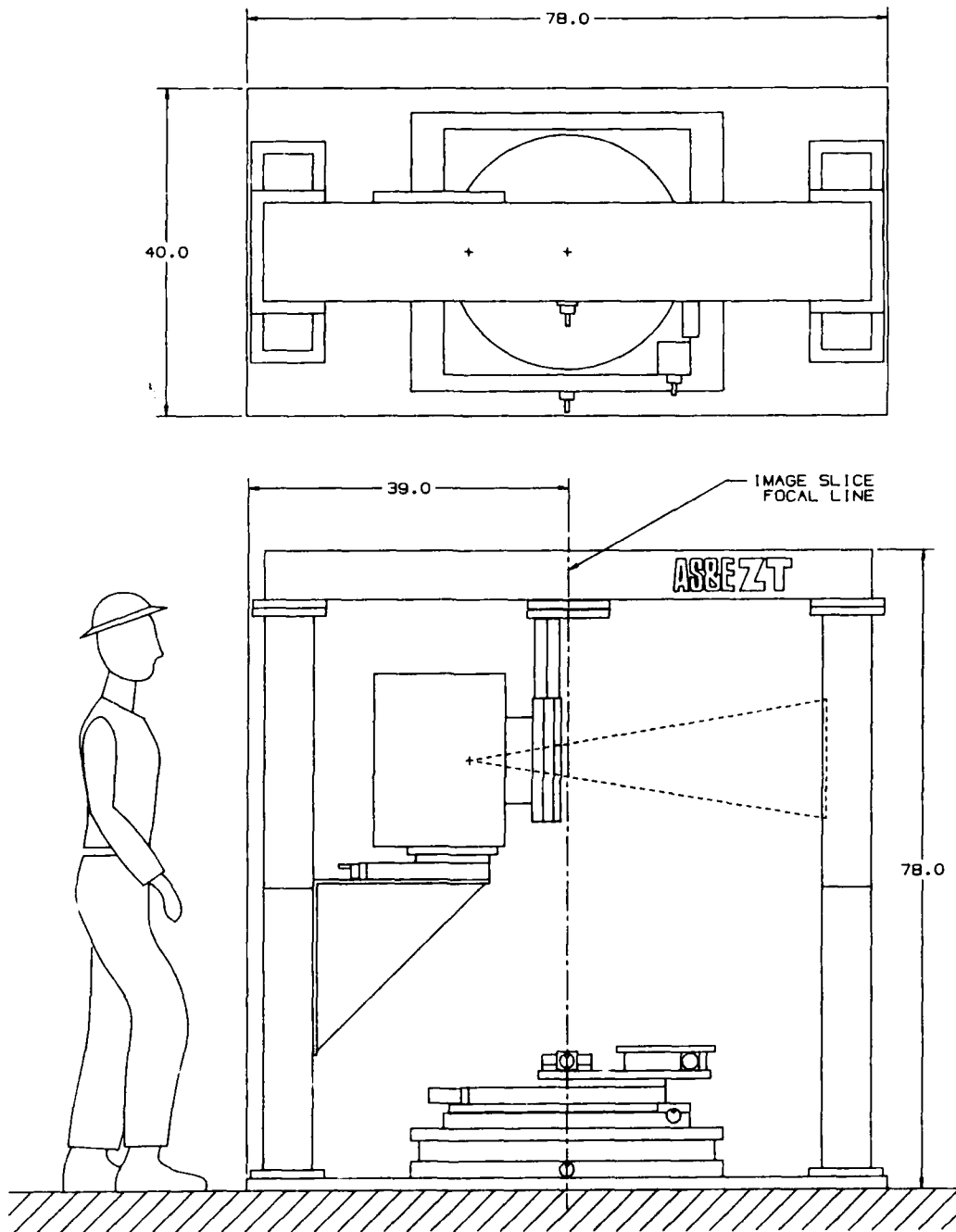


Figure 19. Phase II System Mechanical Hardware Layout.

The ZT collimator and detectors are the components which generate the "slice" backscatter images. The collimator absorbs all the scattered X-rays produced by the primary beam except those that are generated at some fixed distance from the front of the collimator. The depth of this region of acceptance, combined with the width and height of the pencil beam, defines a volume element (voxel) that generates the only scattered X-rays which can be detected by the backscatter detectors. This is illustrated in Figure 20.

The concept shown envisions two ZT collimator/detector pairs which can be independently rotated about a common focal line. This will allow the system to be used to inspect both cylinders and flat objects at a range of primary beam incidence angles. For cylinders, the incidence angle can be varied from 90° to the surface to tangential to the surface. For flat objects, it can be varied from 90° down to approximately 25° . These are illustrated in Figures 21 and 22.

The advantage gained in going to shallow incidence angles has to do with how the voxel mentioned above is formed. Two of the three voxel dimensions are formed by the primary beam precollimator and the third is formed by the ZT collimator. In general, the two controlled by the precollimator will be smaller than the one controlled by the ZT collimator. In the test setup, the former was 0.040 in., the later 0.120 in.. The slice thickness in the image will depend upon how the object is moved relative to this illuminated voxel. Moving parallel to one of the 0.040 in. dimensions will result in a 0.040 in. slice and moving parallel to the 0.120 in. a 0.120 in. slice. It is clear that the image of a delamination between the layers of a composite structure will be vastly better with the 0.040 in. slice. Achieving this gain requires the ability to shoot as near to tangential to the test object as possible.

The range of test object motions required is achieved through use of the series of translation, rotation and elevation stages shown in Figures 17 and 18. The manual elevation stage sets the vertical position of the slice to be taken. It will be designed with a stroke of one half of the maximum test article height, scanning the lower half of a large object will require that it be flipped. Mounted on top of the elevator is a manual rotary stage which is used to set the incidence beam angle. Next is a motorized translation stage

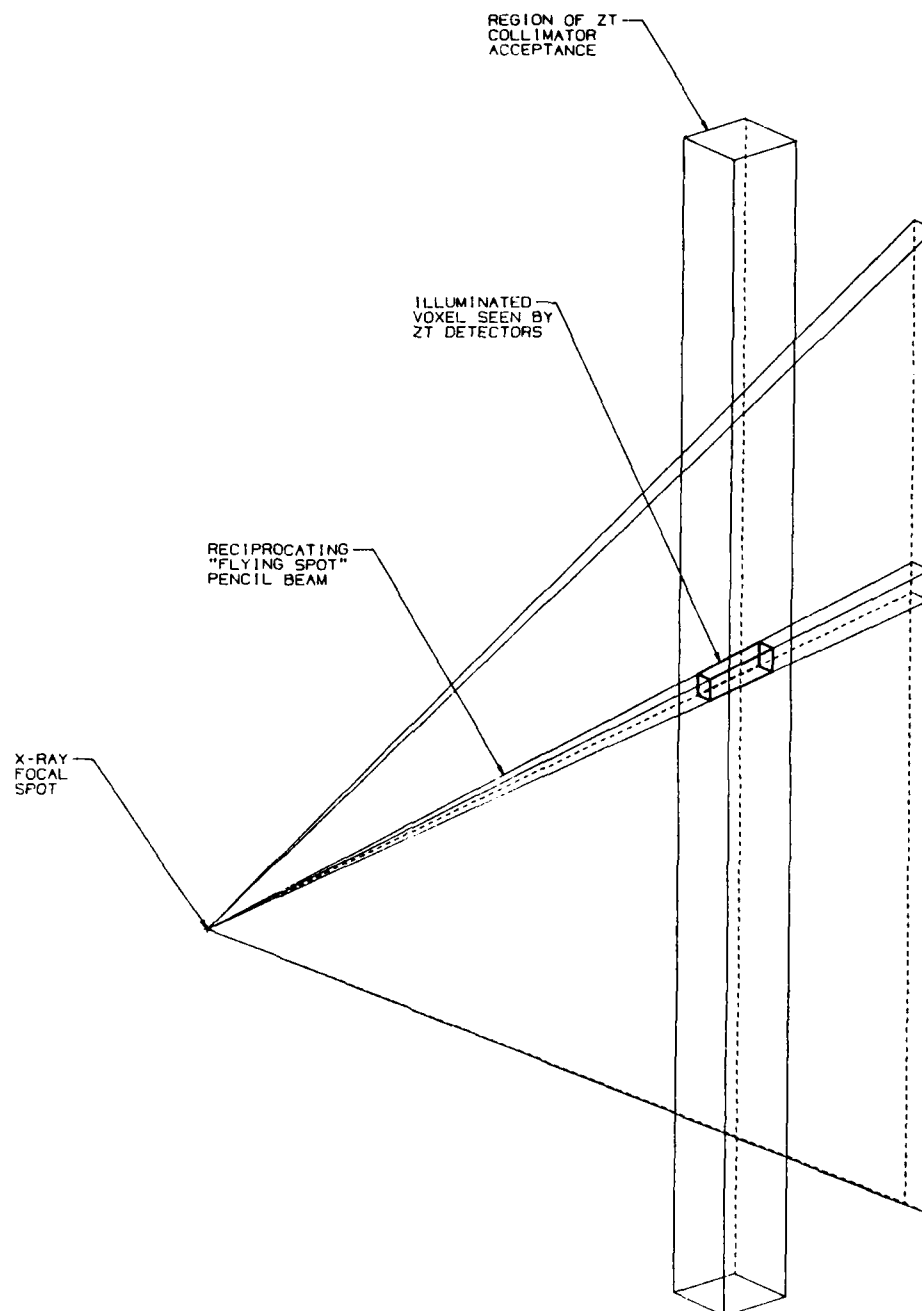


Figure 20. ZT "Voxel" Generation

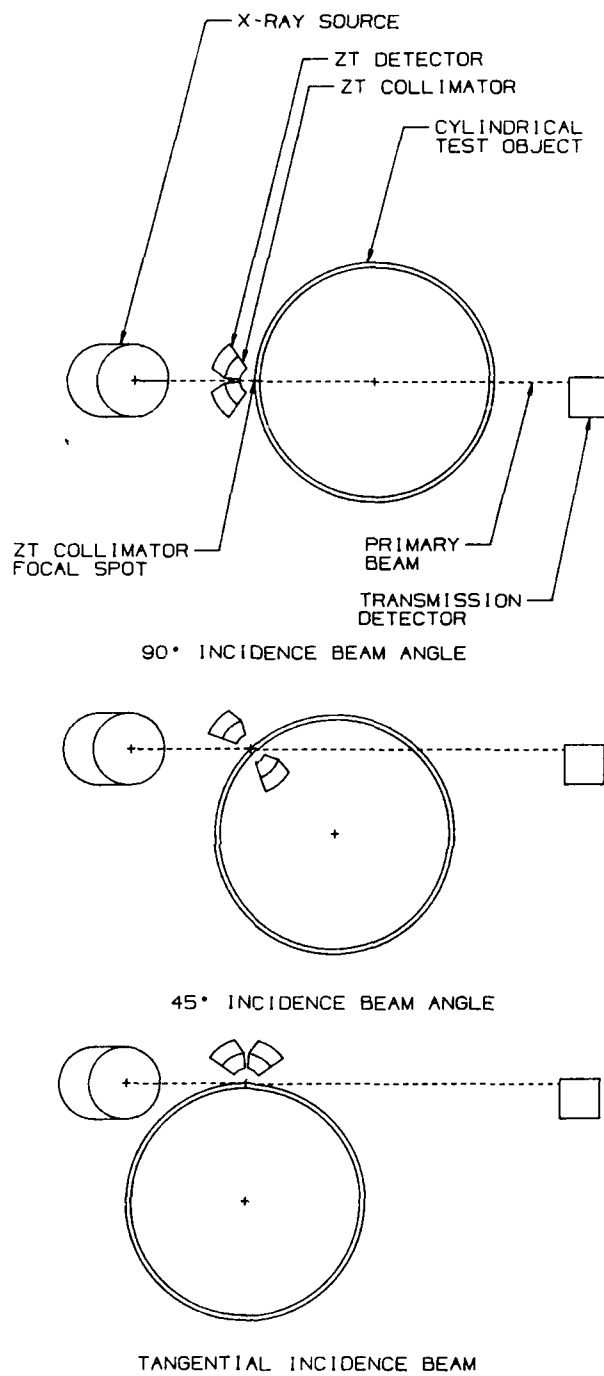


Figure 21. Inspection Geometries

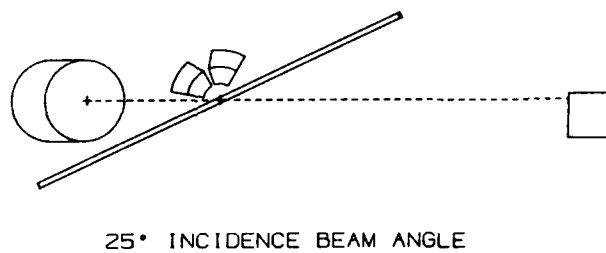
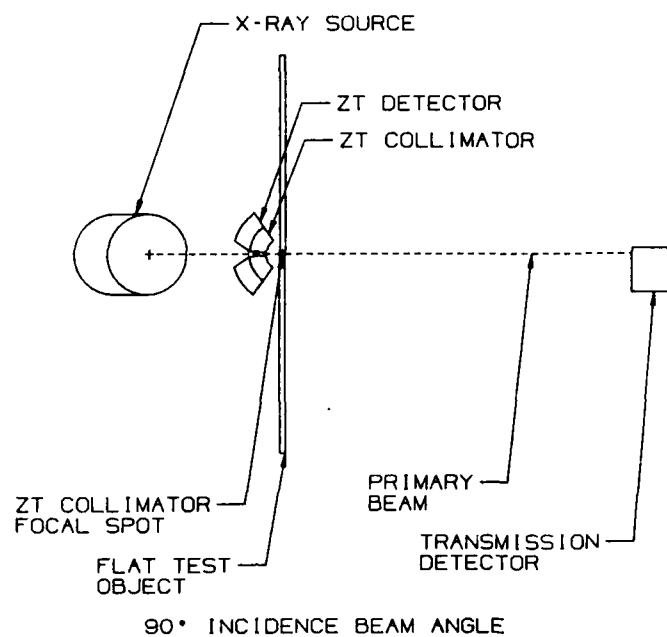


Figure 22. Operational Setup for Flat Plate Objects at Various Incidence Beam Angles.

which serves two different functions. For scanning flat objects, it is used to generate the translation motion, for cylinders it sets the depth of the slice in the test object. Finally, on top this stage are a manual translation stage for setting depth of slice for flat objects and a motorized rotary stage for generating the rotary motion for cylindrical objects.

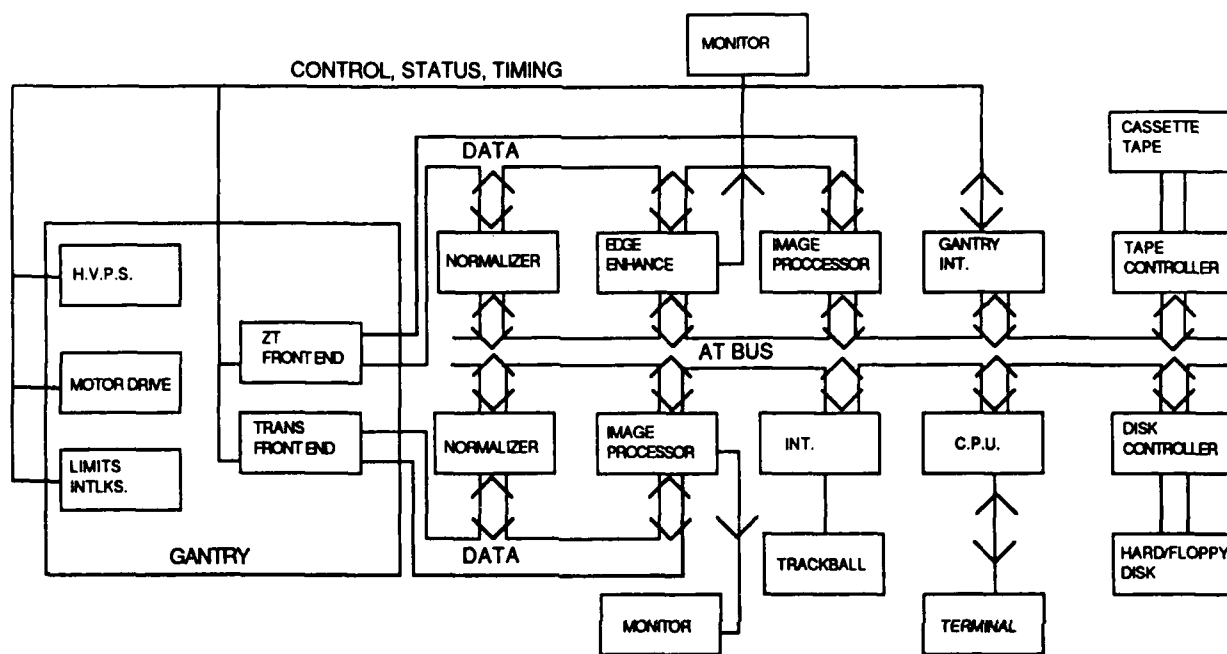
The dimensions chosen for the preliminary conceptual design are based on a system for inspecting objects up to 36 in. high, 24 in. in diameter and 1 in. thick. These in no way represent any fundamental limit of ZT technology. Instead, they were chosen so that a broad range of test objects could be scanned while still keeping the equipment a reasonable size. With the appropriate modifications, larger objects could easily be scanned.

Data Acquisition and Display

The data acquisition will consist of two separate but similar channels, one for ZT and one for transmission. Each channel contains a data acquisition front end electronics as described, interfaced to its own image processor board, and a "PC" type computer.

Each image processor board is capable of storing and displaying four 512 x 512 images with provisions to scroll between images in the corresponding board. The ZT channel will do an edge enhanced image in parallel with data collection of the original image and store it as one of the four images. The operator will interact with the system through a computer terminal and trackball with function switches for single stroke operations.

The scanner will be interfaced to the computer to accomplish control such as turn on X-rays, start scan, etc., and monitor status such as interlocks, system ready, etc., as shown in Figure 23.



SYSTEM DATA BLOCK

Figure 23. Systems Data Block Diagram

The data acquisition front end contains detector, interchangeable logarithmic and square root preamplifiers, an integrator, sample and hold, and analog to digital convertor. A digital to analog convertor is used to introduce normalization data into the data stream. Tri-state registers allow bi-directional communication to the data buss. This is shown in Figure 24.

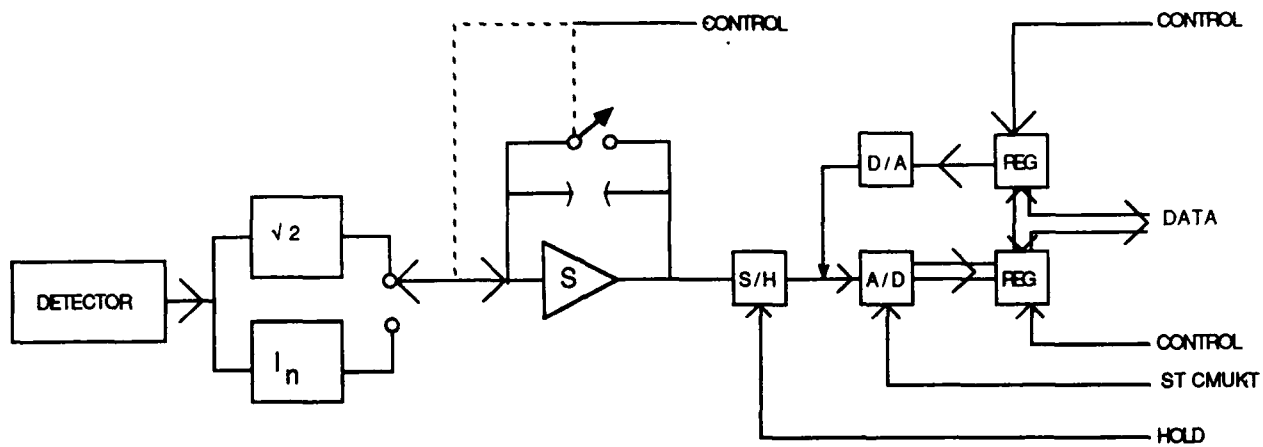


Figure 24. Data Acquisition Front End

PROJECTED PERFORMANCE

Projected Performance of the Phase II Conceptual Design

The proposed Phase II system differs from the existing laboratory system in several fundamental ways. The new geometry will yield more X-ray flux at the imaging plane and will have a much sharper beam profile. A new X-ray tube will allow more X-ray flux to be used in the inspection and a collimator specifically designed for this application will all contribute to added sensitivity for the detection of defects. Each of these contributions will be discussed individually.

X-Ray Flux

There are two major contributions to an increase in the X-ray flux that can be used in this system. The first is the new geometry and the second is the utilization of a new X-ray tube with higher continuous current capability.

The X-ray tube used in the Phase I experiments was limited to 10 mA continuous anode current. The tube proposed for Phase II has 30 mA continuous current capability. This will allow for an increase in the available flux of a factor of three. This will account for an increase in system sensitivity to detection of flaws of about 70%.

The proposed geometry is designed specifically for the applications that are of interest to AFAL. It allows a much smaller distance from the X-ray tube focal spot to the inspection plane. It also allows a much smaller distance from the beam defining aperture to the inspection plane. These two distance reductions result in higher X-ray flux and a more sharply defined pencil beam. The distance from the focal spot to the inspection plane in the laboratory system is 26.375 in. In the proposed Phase II system the distance is reduced to between a maximum of 12.75 in. to a minimum of 10.5 in. Since the flux at any distance from the focal spot of the tube is inversely related to the square of the distance, this means an increase of between 4.3 to 6.3 in the amount of

available flux at the inspection plane. This will increase the sensitivity of the system by a little over a factor of two.

ZT Collimator Design

The ZT collimator used during the Phase I research was the collimator that was available at no cost to the program. It was appropriate to the problem but not specifically designed for the AFAL interests. We propose to specifically design a collimator for the Phase II program. It will result in a thinner slice thickness and increase collection area. The thinner slice thickness has two important impacts. It decreases the out of plane double scatter that is detected and increases the contrast of sub-millimeter size defects. Both of these affect the signal to noise and the detectability of defects. The combined effect of these two changes is to increase the detectability by the order of 40%

Pencil Beam Geometry

The Phase II geometry has a marked affect on the profile of the beam at the location of the inspection plane. At the beam defining aperture the beam profile is a square beam with very sharp edges. As the beam travels from the defining aperture to the inspection plane, two effects change its shape. First the beam gets larger simply because of magnification. Secondly, the edges tend to blur because of the finite focal spot size of the X-ray tube. Figure 25 shows the beam profile of the laboratory system that was used to obtain the data in Phase I and the beam profile of the proposed Phase II system both at the inspection plane. Note that the proposed beam profile is much sharper with well defined edges. The Modulation Transfer Functions (MTF) of these two profiles are shown in Figure 26. Note that for the same beam aperture the MTF of the proposed system is higher at all frequencies and has a higher first zero frequency.

This is technically of interest but does it really affect the detection of defects? The answer to that question is definitely yes. Figure 27 shows the expected intensity profile as the beam profiles of Figure 25 scan over an

BEAM SHAPES AT TOMOGRAPHIC PLANE

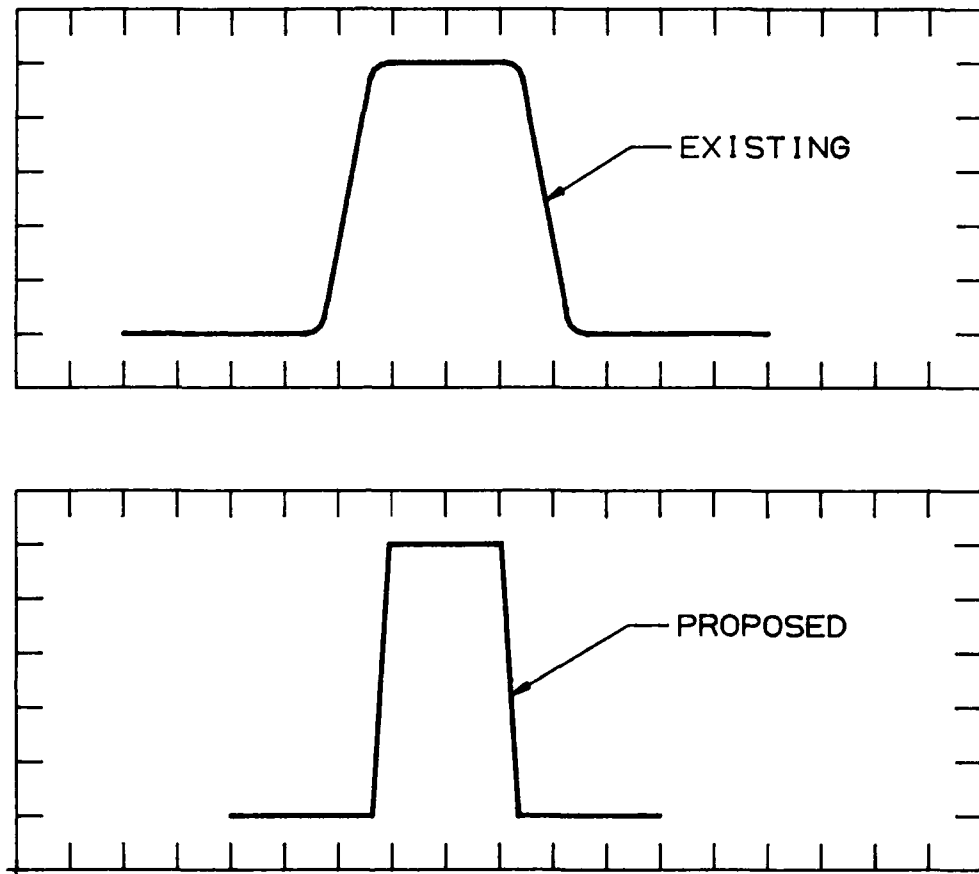


Figure 25. This figure shows the X-ray beam profiles at the inspection plane for both the Phase I system (existing) and the proposed Phase II system. These shapes assume the beam defining aperture size. The greater width for the existing profile occurs because of the greater optical magnification in the Phase I system. The rounded corners in the existign profile are the effect of the finite size of the X-ray tube focal spot. The proposed beam profile will produce superior images.

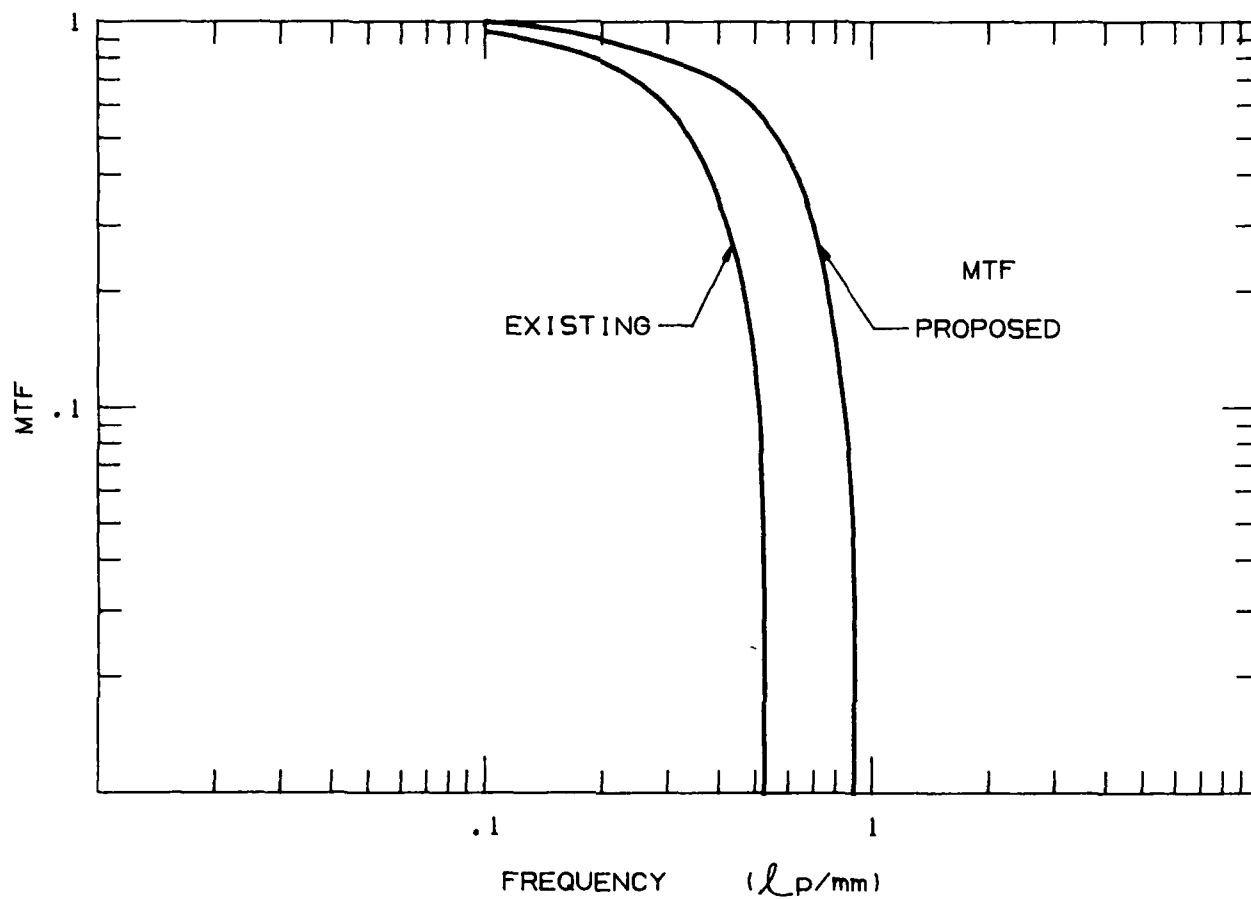


Figure 26. The Modulation Transfer Function (MTF) for the existign and proposed systems for equally sized beam defining apertures. The MTF is a general measure of the quality of a system. Larger values of the MTF at any given frequency will result in a better image. The Phase II system is superior at all frequencies and has a significantly greater first zero.

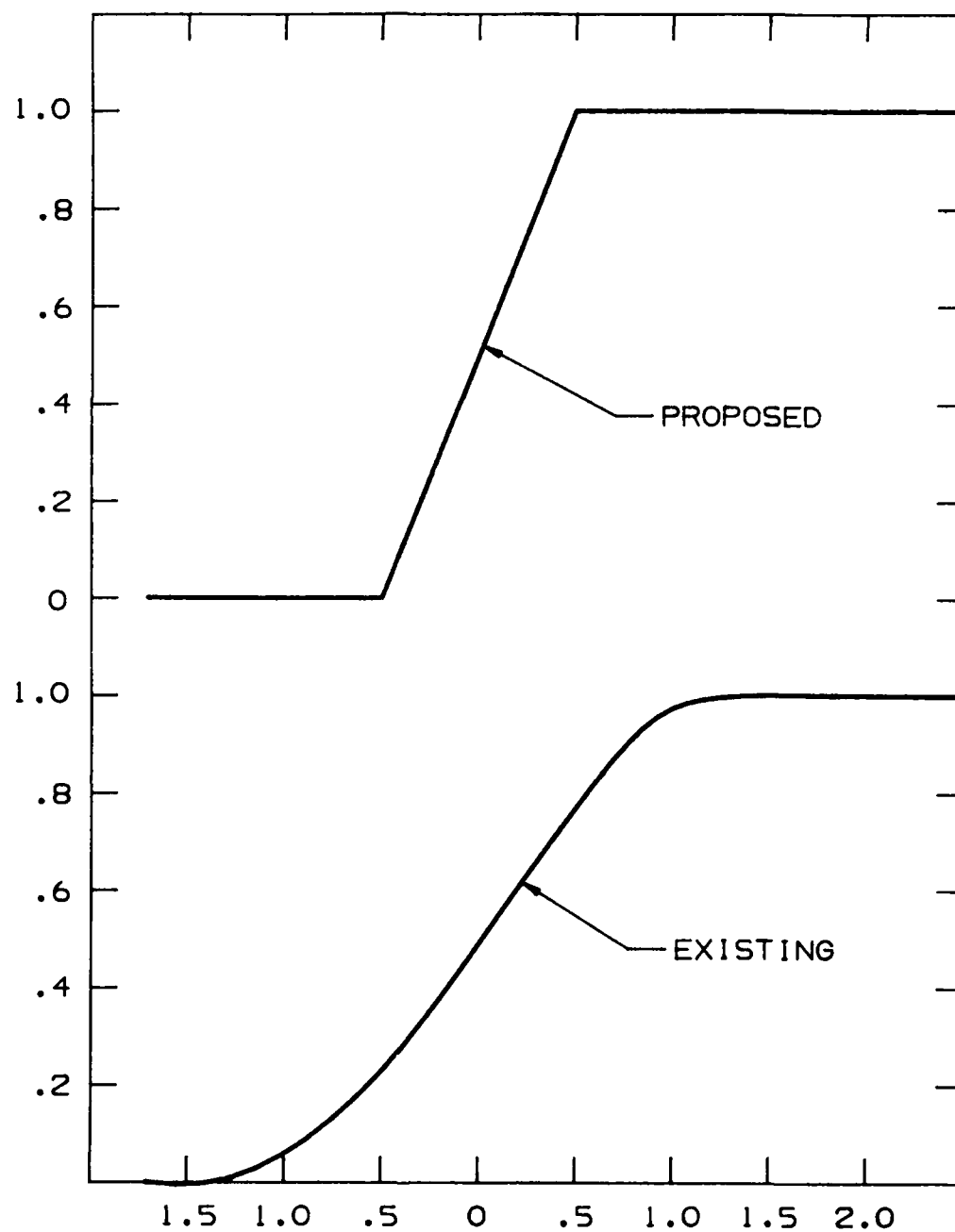


Figure 27. This shows the theoretical output signal from the backscatter detectors as the proposed and existing beam profiles scan over an edge. The increased slope and sharper corners of the proposed edge response function will result in better defect detection.

opaque edge. Two things are apparent. First the proposed system has sharper edges at the transitions and second the slope of the transition is greater by a factor of 1.74. Other imaging sciences have attempted to quantify the effect of the slope of edges on the detectability of defects. A good reference from medical X-ray imaging is **Conspicuity and Uncertainty in the Radiographic Detection of Lesions** by George Revesz (Radiology 1985; 154:625-628). The term conspicuity here is very similar to a generalized signal to noise ratio and is useful to predict the probability of detection. They found that the slope of the edge of the defect in the image (they use the term gradient) is linearly included in the calculation of conspicuity. Therefore for sharp edged defects, the detectability will be increased by an amount which is equivalent to an increase in the signal to noise of about 1.7. Note however that this type of analysis does not apply to defects which have soft edges of the order or greater than one millimeter.

Effect on Detectability

The overall effect of all of the above is to effectively increase the signal to noise ratio by a factor of about 8. This analysis then suggests that sharply defined delaminations of the order of 1 cm in diameter could be detected when the delamination is of the order of 25 microns (0.001 in.). Porosities or generalized density variations (where the effect of sharp edges will not be applicable) should be visible when the change in density is 1.0% over areas of 1 cm².

APPENDIX A

ZT: A TOMOGRAPHIC BACKSCATTER TECHNIQUE FOR NONDESTRUCTIVE EVALUATION

Martin Annis and Paul Bjorkholm
American Science and Engineering, Inc.
Cambridge, Massachusetts

Abstract

A new X-ray imaging technique has been developed at AS&E which has unique capabilities. It is a tomographic, backscatter system called ZT. The technology is intrinsically one-sided, images thin slices of the object under inspection parallel to the front surface of the object, and is sensitive to the electron density of the material. The technique consists of a scanning beam of radiation appropriately chosen for the application, combined with a highly efficient collimator and X-ray detector system. The system is particularly sensitive to delaminations within the first ten or twenty centimeters of the material. Not only is the system more sensitive to the detection of delaminations than CT but because of the display, operators will perceive the delaminations more easily and at a smaller size. The technique is also particularly sensitive to water within structures. It can detect amounts of water that are as small as 0.1 cubic centimeter within composite materials. A laboratory system is described in detail, compared to CT, and applications of the technique to nondestructive evaluation will be given with quantitative results.

PRINCIPLE OF OPERATION

The technique requires two separate components, a source of scanning radiation and a collimated detector. The source produces a well defined pencil beam of radiation that can be moved within a fan shaped region. This is shown schematically in Figure 1. If the radiation backscattered from the object were measured, the signal would be related to the scatter cross-section as integrated along the line of sight into the object times the

flux at the given depth. Then, if a collimated detector is added, it is possible to differentially measure the scatter cross-section at a given depth in the object. This is shown in Figure 2. Here, the view is from the top. The collimator consists of multiple channels defined by x-ray attenuating material. In an apparatus we have constructed, each channel has parallel sides and is designed such that the projections of the sides intersect the plane defined by the scanning beam to define a slice thickness in the beam

plane. The slice thickness and the distance of the intersection from the front of the collimator are design parameters. The detector can only see scatter originating from this volume of intersection. Since the illuminating radiation is in the form of a pencil beam, only a small section of the total volume is illuminated at one time. Therefore, the detector responds only to radiation scattered from that small sub-surface section of the object. As the beam is scanned, the total sub-surface volume is traced out. If the object is then moved in a direction perpendicular to the plane of the beam (or if the source collimator and the detector are moved relative to a stationary object) at a speed slower than the x-ray scan speed, a slice parallel to the surface is traced out. If one samples the output of the detector repeatedly with a time constant small compared to the time it takes the beam to move over a region of interest, many samples of the scatter from the sub-surface plane may be obtained. These samples can be digitized, stored, and displayed as a visual image of the object. A schematic of a typical system is shown in Figure 3.

We have constructed a collimator which has the property of collecting scattered radiation with extremely high efficiency. This collimator is made up of flat planes. The collimator has the property that it may remain fixed as the flying spot moves parallel to the planes of the collimator. The principle disadvantage of this collimator is the fact that double scattering events originating from primary scattering interactions by the pencil beam not in the slice plane cause extraneous signals. The thinner the slice, the smaller is this effect. We have also designed a conical collimator which minimize this effect.

THEORY

X-rays interact with matter via a number of different phenomena. These are principally the photo-electric effect, pair production, and Compton scattering. Some minor interactions will not be addressed here but can be found in the literature.

The photo-electric effect causes the removal of an x-ray photon from the beam with the energy converted into kinetic energy of an electron and, sometimes, lower energy fluorescent photons. The detailed energy conversion depends upon the atomic number of the material (Z). The fluorescent radiation from the slice is also detected and may be important for high Z materials.

X-rays at an energy much greater than 1 MeV can interact with matter by pair production. Here the photon energy is converted into a pair of particles consisting of an energetic electron and an energetic positron. The positron will eventually annihilate with an electron and yield a pair of 511 keV photons.

Compton scattering is caused by scattering of an x-ray photon by a nearly free electron. The energy of the scattered photon depends upon the energy of the incident photon and the angle of scatter. This effect can also be used to cast shadows in projection radiography but the scattered radiation causes a non-imaging background which is troublesome for most radiographic imaging systems. For example, in conventional radiography of human abdomens the flux of x-rays directly at the exit from the body is dominated by scattered radiation. Thus, successful diagnostic radiography of the human abdomen requires some form of scatter rejection.

As the energy of the incident photon increases, the average angle of scatter moves forward. However, even at very high energies

some photons are scattered in the backwards direction. The differential scattering cross-section per unit solid angle is given by the well known Klein-Nishina formula.

This general review of interaction types between X-rays and matter is necessary because the type of imaging described here utilizes principally Compton scattered photons. For materials of high atomic number, the photo-electric effect will produce fluorescent K-shell photon emissions which occur with a high probability and which may also be used for ZT imaging. For the higher energies and/or the lower range of atomic number (Z), Compton scattering dominates. Figure 4 shows the region where the photo electric effect, Compton scattering, and pair production predominate (1). For most materials, Compton scattering is the dominant process from 100 keV to 10 MeV. For lower Z materials, the lower energy limit is further depressed. This range of energies and Z values includes most of the region of interest for radiography, including medical applications. However, there are particular applications where the higher Z materials can be most effectively imaged by their fluorescence.

We will consider a typical application of the ZT technique with a convenient geometry which we have employed (see Figure 5). In this geometry which is relatively simple to calculate approximately, the pencil beam of x-rays is incident normal to the surface of the object. Although 180° backscattering offers the lowest differential cross-section, and the scattered photon has the lowest energy at 180°, our calculations indicate this is an optimum geometry at all photon energies because (1) it allows the source to be closer to the object giving a greater flux, and (2) the path length of X-rays into the object is minimized. In this geometry, the back scatter detectors are placed on

either side of the pencil beam plane as shown in Figure 2. In these calculations we assume that the input beam of photons is mono-energetic. For a polychromatic spectrum the equations below may be integrated over the input energy range. The scattered flux per unit area in the slice I_s (photons/cm²) is given by:

$$I_s = I_0 e^{-\mu_0 x} \int_{\Omega} \frac{d\sigma}{d\omega} \frac{NZ}{A} \Delta x e^{\frac{-\mu' x}{\cos(\pi-\alpha)}} T(\alpha) d\Omega \quad \text{Equation 1}$$

- where
- I_0 = incident flux (photons/cm²)
 - μ_0 = total attenuation coefficient of incident x-ray (cm²/g)
 - x = depth of slice (g/cm²)
 - Ω = the solid angle subtended by the collimator at a typical point in the ZT slice. For ease of calculation, we have assumed that the excursion of the pencil beam across the slice is very much smaller than the height of the collimator. Thus Ω is assumed to be constant.
 - α = angle between incident x-ray and scattered x-ray
 - $\frac{d\sigma(\alpha)}{d\omega}$ = Klein-Nishina differential scattering cross-section, which depends upon the incident photon energy and the angle which in turn determines the scattered photon energy (cm²/electron).
 - N = Avogadro number = 6×10^{23} atoms/molecular weight
 - Z = atomic number
 - A = molecular weight (g)
 - Δx = thickness of slice (g/cm²)
 - $\mu'(\alpha)$ = the total attenuation coefficient of scattered photons (cm²/g), which depends on α .
 - $T(\alpha)$ = the transmission of the collimator.

ϵ_{det} = efficiency of detection of the scattered photons (assumed to be $\sim .3$)

The factor $e^{-\mu_0 x}$ in Equation I is the attenuation of the incident beam prior to reaching the ZT slice depth. Since this factor multiplies the factor which expresses the scattering from the slice, the resultant image density will be modulated by the overlying material. Thus, the ZT image does not give an absolute quantitative measure of the density within the slice as does a CT image. However, since the factor is multiplicative, geometrical shapes are easily understood and diagnosed.

The factor $e^{\frac{-\mu'(\alpha)x}{\cos(\pi-\alpha)}}$ which appears under the integral is due to the attenuation of the scattered photons exiting the object. This involves an integration over the total solid angle and averages over large areas thereby reducing local overlaying density variations. In many industrial or medical applications the material overlying the ZT slice is very close to a constant thickness and composition so that quantitative density measurements may be achieved. Table I tabulates some useful parameters for several energies and angles of scattering. Note that the energy of the backscattered photons are kinematically limited. At 180° the scattered photon energy asymptotically approaches 255.5 keV. For the collimator and detector we have constructed $\Omega \approx 3$ steradian. Then Equation I becomes (approximately):

$$\frac{I_s}{I_0} = 4.15 \times 10^{22} \frac{d\Omega}{d\omega} e^{-\mu_0 x} e^{\frac{-\mu' x}{\cos(\pi-\alpha)}}$$

Equation II

where

$$\begin{aligned}\bar{\alpha} &\approx 150^\circ \\ \epsilon_{\text{det}} &\approx 0.3 \\ T(\alpha) &\approx 0.6\end{aligned}$$

$Z/A = 0.48$. Z/A is approximately constant over the periodic table and has been chosen to be that of Al.

$x = 1 \text{ g/cm}^2$ which is equivalent to 1.3 mm of Fe , 3.7 mm of Al or 10 mm of plastic. The result may be easily scaled to other slice thicknesses.

Figure 6 shows an evaluation of Equation II for various materials where the ordinate N_s , the number of scattered photons per cm^2 per milli-Roentgen of incident radiation is plotted as a function of the energy of the incident photon, E_0 for various amounts of overlaying material. The general features can be easily understood in terms of the physics involved. The monotonic decrease in the number of scattered photons at high energies reflects the decrease as a function of energy of the Compton cross section. The rapid decrease at low energies that depends on the Z of the material is caused by the increase in the photo-electric cross-section as energy decreases.

Suppose, for example, one wishes to penetrate 5 cm of soft tissue (approximately 5 g/cm^2 of nitrogen) and achieve a 1 cm ZT slice. From Figure 6, it is clear that an x-ray peak energy of about 100 keV would be suitable and would result in a scattered flux of about $6000 \text{ photons/cm}^2 \text{ mR incident}$. In our laboratory we have achieved 10 mR incident over a field measuring about 12 cm x 12 cm, in a period of 10 seconds, with a pencil beam 1 mm x 1 mm. The corresponding spatial resolution for a flying spot system may be shown to be one line pair per millimeter.

Using an incident flux of 10 mR, there would be about $6 \times 10^4 \text{ photons/cm}^2$, giving a one sigma standard deviation noise to signal of 0.4% per cm^2 or 4% per mm^2 . The images we

have achieved in our laboratory approximately affirm these estimates.

Consider first the problem of imaging a very thin object. Using conventional projection radiography, one would wish to utilize a low keV energy beam to improve contrast. This would be impossible if the thin object had a relatively thick structure behind it that had to be penetrated. The object would then have to be x-rayed with a high-energy beam, thus reducing contract resolution, even at high X-ray energies. This is because only those photons which interact in the thin object are detected, resulting in a very large statistical signal-to-noise.

Figure 7 shows an example of a thin object. An automobile dashboard was given to us for evaluation. It consists of a metal base, 1/4" to 5/8" of low density foam, and a vinyl covering. The manufacturer was interested in detecting voids in the foam under the vinyl. Standard projection radiography could not demonstrate the void because the low density foam provided inadequate contrast. Backscatter radiography was also unable to demonstrate the void because of the very large scatter signal from the metal base. However, a ZT slice through the defect visualized the void with very high signal to noise. The increased signal to noise (as compared to standard backscatter imaging) is a result of the reduction of signal from scattering mass in front of and behind the ZT slice without any reduction in the signal from the void within the slice. This therefore represents a case where the material of interest is thin radiographically.

On the other hand, when the object is very thick and the defect to be imaged is a delamination, ZT has two very important advantages over CT. First, the defect is displayed en face. That is, for a 1 cm x 1 cm x 0.025 cm defect, the defect appears 1 cm x 1 cm in the

ZT image. It is easily detected and its spatial extent is quickly and naturally seen and appreciated. While the thickness of the delamination is not immediately obvious, the intensity of the signal is proportional to the mass defect.

A CT display of the same defect would be a line of pixels 1 cm long. Since, for most CT systems a 0.025 cm crack would be very much smaller than a pixel size, imaged crack width would be one pixel. Only one dimension would be displayed, the length of the object in the plane. The out of plane dimension could be determined only with multiple slices.

Figure 8 shows the displays one expects from ZT and CT of similar defects. Note that one appreciates different aspects of the delamination in the two images. Figure 8 (a) shows a 0.040" delamination in a large object utilizing a CT reconstruction using data taken with a 16 MeV X-ray spectrum. There is a clear and obvious change in the image at that location. Figure 8 (b) shows a ZT image of a phantom which duplicates the densities and thicknesses of the object in (a) but is smaller and could be scanned on the laboratory ZT machine. Mass defects as thin as 0.005" (127 microns) are easily seen and their dimensions appreciated. These data were taken with a 110 kVp X-ray spectrum. This is an example of the power of this one sided perpendicular viewing X-ray modality.

References

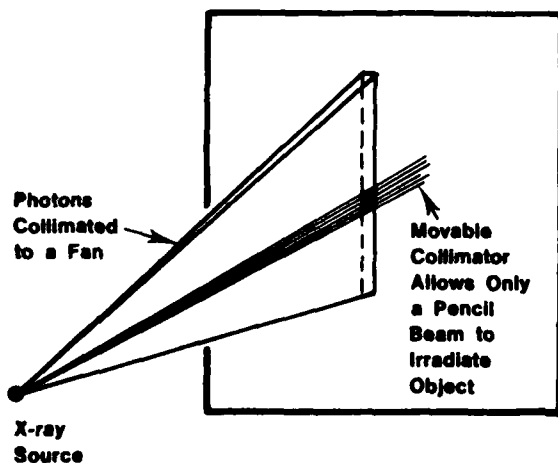
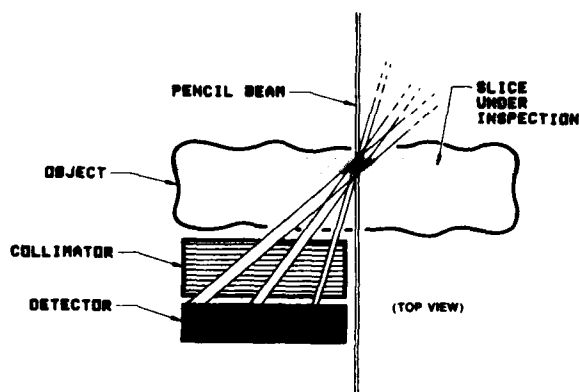
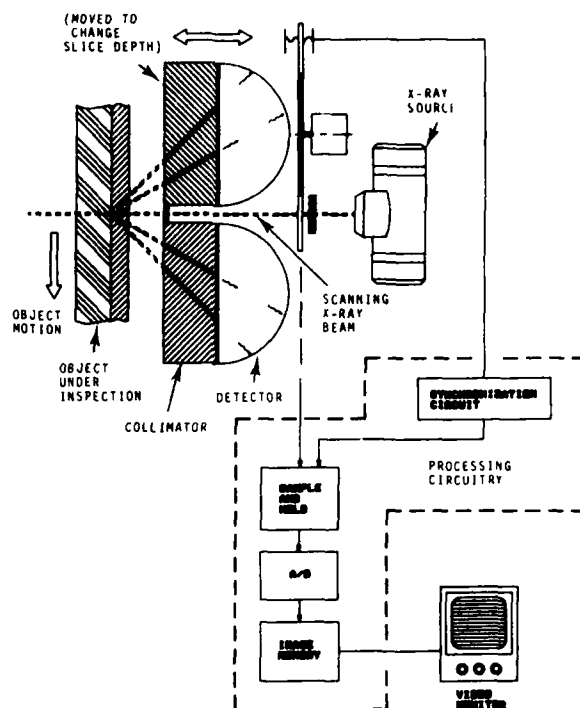
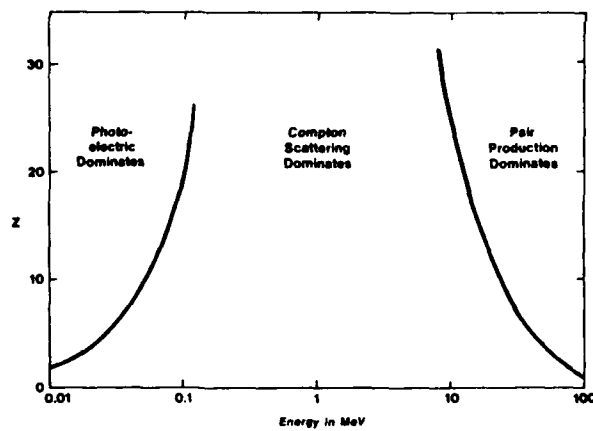
1. Evans, R.D. 1955. The Atomic Nucleus (New York: McGraw-Hill).
2. McMaster, W.H., et al. 1969. Compilation of X-Ray Cross Sections. (UCRL 50174 Sec. II, Rev. 1, Lawrence Livermore National Laboratory, University of California).
3. A.I.P. Handbook, 1972. New York: McGraw Hill.

ACKNOWLEDGMENTS

The authors would like to thank Mike Johnson for his help in design of the system.

TABLE I

Photon Energy Incident	Photon Energy 135°	Scattered at 180°
100 keV	75 keV	72 keV
1000	230	204
10000	290	249

Figure 1
Scanning x-ray beam techniqueFigure 2
Schematic indication of how the linear collimator and pencil beam define a sub surface slice.Figure 3
The ZT imaging system schematic.Figure 4
The three major x-ray interaction processes vary in probability with both atomic number and energy. The two heavy lines indicate the locus where the indicated process cross sections are equal. Note for low Z materials, Compton scattering dominates over a wide range of energy.

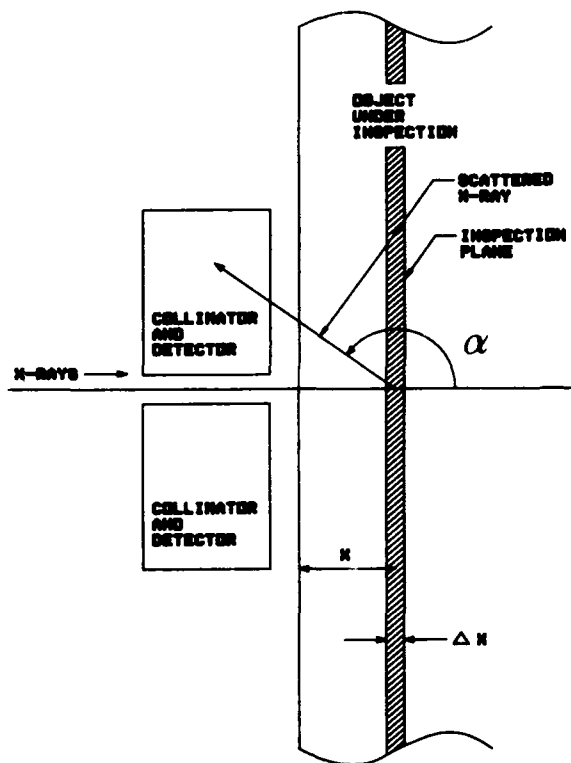


Figure 5
ZT system geometry which produces near-optimum results.

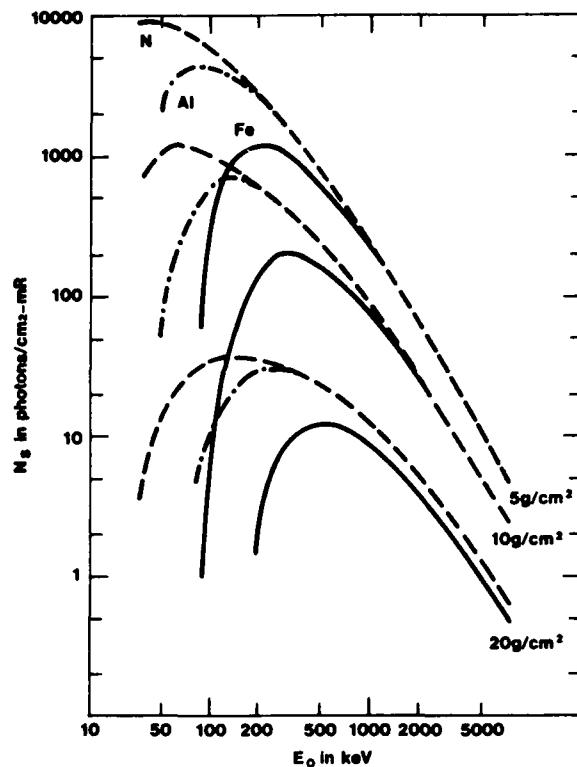


Figure 6
Number of scattered photons detected, N_s , per cm² and per milli-Roentgen of incident radiation as a function of the energy of the incident photon, E_0 , for various materials and depths of slice.

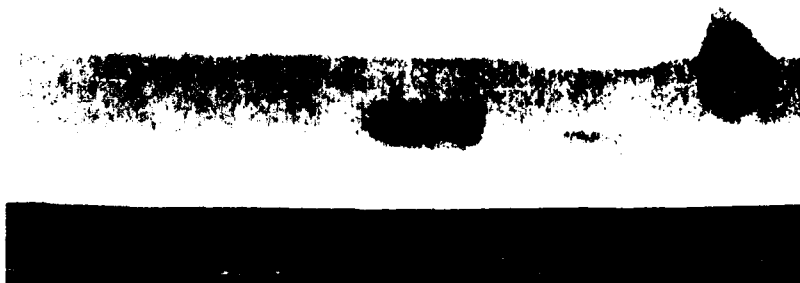


Figure 7

The top image is a photograph of a dashboard inspected by ZT as shown in the bottom image. The void in the foam is obvious in the ZT image. A projection radiograph doesn't show the void because of the very low radiographic density. A non-tomographic backscatter image doesn't show the void because of the overwhelming scatter from the metal back.

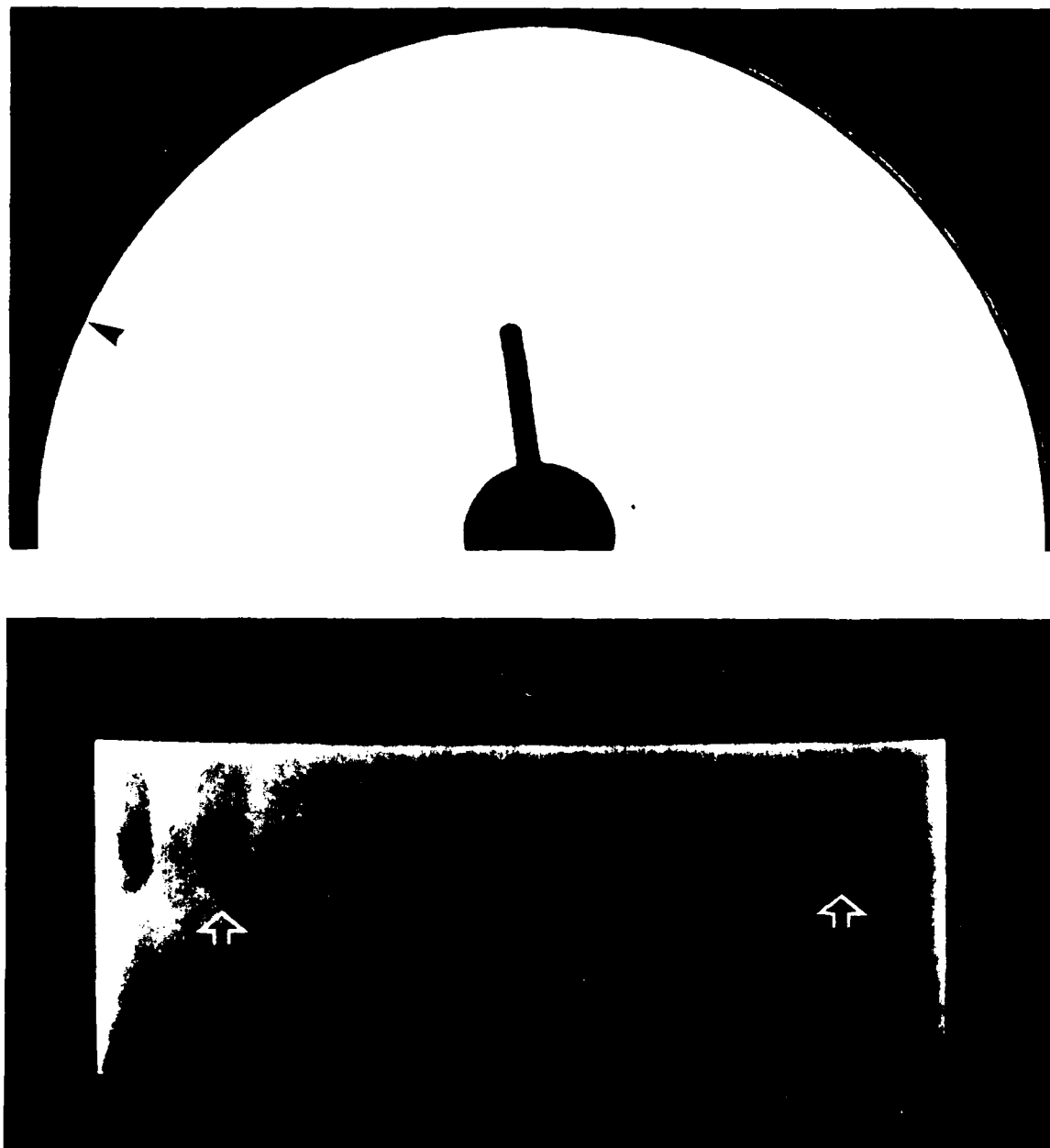


Figure 8

(a) A CT reconstruction of a phantom with a manufactured delamination of 0.040" thick (black arrow). Note the defect appears as a narrow short line. (b) A ZT reconstruction of a series of manufactured delaminations of 0.080, 0.040, 0.020, 0.010, and 0.005" thick, with two different frontal areas. The case thickness and densities are as in (a). The two white arrows note 0.040" delaminations. Note the ease of detection compared to CT. The 0.010" delaminations are easily seen in the original display. The delaminations decrease in the thickness from both edges to the center.

END

DATED

FILM

8-88

Dtic